J. Fluid Mech. (2009), *vol.* 634, *pp.* 5–39. © 2009 Cambridge University Press
doi:10.1017/S0022112009990516 Printed in the United Kingdom

Prediction of vortex-induced vibration response by employing controlled motion

T. L. MORSE AND C. H. K. WILLIAMSON†

Sibley School of Mechanical and Aerospace Engineering, Cornell University,
Ithaca, NY 14853, USA

(Received 6 November 2008 and in revised form 18 May 2009)

In order to predict response and wake modes for elastically mounted circular cylinders in a fluid flow, we employ controlled-vibration experiments, comprised of prescribed transverse vibration of a cylinder in the flow, over a wide regime of amplitude and frequency. A key to this study is the compilation of high-resolution contour plots of fluid force, in the plane of normalized amplitude and wavelength. With such resolution, we are able to discover discontinuities in the force and phase contours, which enable us to clearly identify boundaries separating different fluid-forcing regimes. These appear remarkably similar to boundaries separating different vortex-formation modes in the map of regimes by Williamson & Roshko (*J. Fluids Struct.*, vol. 2, 1988, pp. 355–381). Vorticity measurements exhibit the 2S, 2P and P + S vortex modes, as well as a regime in which the vortex formation is not synchronized with the body vibration. By employing such fine-resolution data, we discover a high-amplitude regime in which two vortex-formation modes overlap. Associated with this overlap regime, we identify a new distinct mode of vortex formation comprised of two pairs of vortices formed per cycle, where the secondary vortex in each pair is much weaker than the primary vortex. This vortex mode, which we define as the $2\mathrm{P}_{OVERLAP}$ mode ($2\mathrm{P}_O$), is significant because it is responsible for generating the peak resonant response of the body. We find that the wake can switch intermittently between the 2P and $2\mathrm{P}_O$ modes, even as the cylinder is vibrating with constant amplitude and frequency. By examining the energy transfer from fluid to body motion, we predict a free-vibration response which agrees closely with measurements for an elastically mounted cylinder. In this work, we introduce the concept of an ‘energy portrait’, which is a plot of the energy transfer into the body motion and the energy dissipated by damping, as a function of normalized amplitude. Such a plot allows us to identify stable and unstable amplitude-response solutions, dependent on the rate of change of net energy transfer with amplitude (the sign of $\mathrm{d}E^*/\mathrm{d}A^*$). Our energy portraits show how the vibration system may exhibit a hysteretic mode transition or intermittent mode switching, both of which correspond with such phenomena measured from free vibration. Finally, we define the complete regime in the amplitude–wavelength plane in which free vibration may exist, which requires not only a periodic component of positive excitation but also stability of the equilibrium solutions.

---

† Email address for correspondence: cw26@cornell.edu

1. Introduction

Vortex-induced vibration is an important problem in many fields of engineering. It affects the dynamics of riser tubes bringing oil from the seabed to the surface, as well as civil engineering structures such as bridges, chimneys and buildings, and is cause for concern in many other practical applications. The range of problems caused by vortex-induced vibration has led to a large number of experimental and computational studies on the subject, including several review papers, for example Sarpkaya (1979), Griffin & Ramberg (1982), Bearman (1984), Parkinson (1989) and more recently Williamson & Govardhan (2004).

We focus on one of the most conceptually simple instances of vortex-induced vibration: the case of an elastically mounted rigid cylinder, constrained to move transverse to an incoming flow, which is often used as a paradigm for understanding more diverse experimental arrangements. For such an arrangement, previous studies (such as Khalak & Williamson 1999) have shown that for systems of low combined mass damping there exist three branches of response as the normalized velocity is increased, namely the initial branch, the upper branch and the lower branch. The transition between the initial and upper branches exhibits a hysteresis, while the transition from the upper branch to the lower branch shows an intermittent switching. For systems of high mass damping, only the initial and lower branches exist, with a hysteretic mode transition between them (Feng 1968). Examples of the two-branch and three-branch responses may be found later in this work (see figure 11).

In the present study, we employ controlled vibration of a body in a water channel flow, where the cylinder is effectively translated with a prescribed sinusoidal trajectory relative to the fluid, to provide a deeper understanding of vortex-induced vibration phenomena for freely vibrating bodies. Initially, we set out to investigate a number of questions, such as the following. What is the cause of the hysteresis between the initial branch and upper branch of response? What causes intermittent switching between the upper and lower branches? What modes of vortex formation can cause vortex-induced vibration? What is the relationship between the modes of vortex formation and the fluid excitation? To what extent can controlled vibration be used to accurately predict the behaviour of a freely vibrating cylinder? We address all of these questions in the present work, as well as expand upon the new results which will be presented.

Before addressing the above questions, we shall briefly introduce an equation of motion generally used to represent the vortex-induced vibration of a cylinder oscillating in the transverse y direction (perpendicular to the free stream) as follows:

$$m\ddot{y} + c\dot{y} + ky = F(t), \tag{1.1}$$

where m is the total oscillating structural mass; c is the structural damping; and k is the spring constant. When the body motion is synchronized with the vortex formation, the cylinder motion $y(t)$ and fluid forcing $F(t)$ are typically well approximated by sinusoidal functions (of course, in controlled vibration, the motion is precisely sinusoidal):

$$y(t) = A\sin(2\pi ft), \tag{1.2}$$

$$F(t) = F_1\sin(2\pi ft + \phi), \tag{1.3}$$

where f is the oscillation frequency. The phase angle ϕ between the fluid force and the body displacement is an important quantity, influencing the energy transfer from fluid to body motion and thereby also the response of the body. In this problem, we

Mass ratio	m^*	$\dfrac{m}{\pi\rho D^2 L/4}$
Damping ratio	ζ	$\dfrac{c}{2\sqrt{k(m+m_A)}}$
Normalized velocity	U^*	$\dfrac{U}{f_N D}$
Normalized wavelength	λ^*	$\dfrac{\lambda}{D}=\dfrac{U}{fD}$
Normalized amplitude	A^*	$\dfrac{A}{D}$
Frequency ratio	f^*	$\dfrac{f}{f_N}$
Transverse force coefficient	C_Y	$\dfrac{F}{\frac{1}{2}\rho U^2 DL}$
Reynolds number	Re	$\dfrac{\rho UD}{\mu}$

TABLE 1. Non-dimensional groups: U is the free-stream velocity; λ is the oscillation wavelength; f is the oscillation frequency; f_N is the natural frequency in water; D is the cylinder diameter; L is the submerged cylinder length; ν is the fluid kinematic viscosity; ρ is the fluid density; and F is the transverse fluid force. The added mass m_A is given by $m_A = C_A m_d$, where m_d is the displaced-fluid mass and C_A is the potential added-mass coefficient ($C_A = 1.0$ for a circular cylinder).

select a set of relevant non-dimensional parameters, which are presented in table 1. In particular, the principal parameters defining the body motion are the normalized amplitude (A^*) and the frequency ratio (f^*) in a flow with normalized velocity U^*. (In the definition of natural frequency f_N used in table 1, we have chosen to use the frequency in the fluid medium of interest (in this case water), which introduces $(m^* + C_A)$ in (1.4) and (1.5) below in place of m^* alone which we would find if we had chosen to use natural frequency *in vacuo*.)

Equations defining the amplitude and frequency of the steady-state response may be derived as follows, following the approach of Khalak & Williamson (1999):

$$A^* = \frac{1}{4\pi^3}\frac{C_Y \sin\phi}{(m^* + C_A)\,\zeta}\left(\frac{U^*}{f^*}\right)^2 f^*, \tag{1.4}$$

$$f^* = \sqrt{\frac{m^* + C_A}{m^* + C_{EA}}}. \tag{1.5}$$

where C_A is the potential added-mass coefficient ($C_A = 1.0$ for a circular cylinder) and C_{EA} is an 'effective' added-mass coefficient due to the transverse force in phase with the body acceleration,

$$C_{EA} = \frac{1}{2\pi^3}\frac{C_Y \cos\phi}{A^*}\left(\frac{U^*}{f^*}\right)^2. \tag{1.6}$$

We refer to (1.4) and (1.5) as the 'amplitude equation' and the 'frequency equation' respectively.

We may also discuss the response equations above in the context of energy considerations. The energy transferred from the fluid to the cylinder motion, over one cycle of oscillation, is given by

$$E_{IN} = \pi A F_1 \sin\phi. \tag{1.7}$$

Thus, the phase angle, ϕ, must be between 0° and 180° to yield positive excitation, and this is a required condition for free vibration to occur. We may note that for a cylinder with prescribed sinusoidal motion, the fluid forcing may be close to (but not precisely) sinusoidal. If we represent the fluid forcing as $F(t) = \{F_1 \sin(\omega t + \phi) + F_2 \sin(2\omega t + \phi_2) + \cdots\}$, then the force component we present in this paper is the one corresponding to the fundamental frequency (ω) given by the magnitude (F_1) and the phase (ϕ). Only this component will make a net contribution to the energy transfer from fluid to body motion. In essence, (1.7) is valid even for non-sinusoidal forcing. The energy dissipated by the structural damping is given by

$$E_{OUT} = 2\pi^2 c A^2 f. \tag{1.8}$$

If the system is oscillating with a constant amplitude and frequency, the energy into the system must exactly balance the energy out of the system, over one cycle, which yields

$$\underbrace{C_Y \sin\phi}_{E^*_{IN}} = \underbrace{\frac{4\pi^3 A^* (m^* + C_A)\zeta}{\left(\frac{U^*}{f^*}\right)^2 f^*}}_{E^*_{OUT}}, \tag{1.9}$$

which is equivalent to a simple manipulation of the amplitude equation (1.4) above. The term $C_Y \sin\phi$ is the force coefficient in phase with velocity, which we define as the ‘fluid excitation’, and this represents a normalized energy into the system, E^*_{IN}, over a cycle. For a free-vibration system oscillating at steady state this must be balanced by the normalized energy out of the system, E^*_{OUT}, related to the combined mass damping of the system and given by the right-hand side of (1.9). The combined mass damping $(m^* + C_A)\zeta$ is a key parameter in vortex-induced vibration, as indicated by its appearance in the amplitude equation (1.4).

Our approach, in this study, is to prescribe the ‘relative’ trajectory of the cylinder through the fluid to be a sine wave and to measure the fluid forces over a wide range of normalized amplitude (A^*) and normalized wavelength (λ^*). One may note that normalized wavelength is equivalent to the parameter $U^*/f^* = U/fD$, which is the flow velocity normalized with the actual oscillation frequency (f), rather than the natural frequency (f_N). We shall use these force measurements, along with (1.9), to make response predictions for a freely vibrating cylinder.

In the case of a controlled body, which is translated along a sinusoidal trajectory, Williamson & Roshko (1988) observed a set of different vortex-formation modes, existing within certain regimes in a plot of normalized amplitude and wavelength of the body motion. Among the vortex-formation modes they found were a ‘2S’ mode representing two single vortices formed per cycle, a ‘2P’ mode meaning two pair of vortices formed per cycle and an asymmetric ‘P + S’ mode comprised of a pair of vortices and a single vortex, in each cycle. The Williamson–Roshko map of regimes is shown, for example, in figure 3(*b*) later. Ongoren & Rockwell (1988) observed some comparable vortex-formation modes, in the case of a body oscillating in-line with the flow.

In the case of free vibration at high mass damping, Brika & Laneville (1993) found a two-branch response, observing the 2S mode in their initial branch and a 2P mode in their lower branch, which corresponded well with the Williamson–Roshko map of mode regimes. At low mass damping, Khalak & Williamson (1999) were able to superpose their free-vibration response branches on to the map of wake modes, deducing that the initial branch lies in the 2S region, while the upper and lower branches both lie in the 2P region. These modes were confirmed in free vibration by Govardhan & Williamson (2000), employing simultaneous force and wake-vorticity measurements. However, they found that the 2P mode in the upper branch exhibits a secondary vortex in each vortex pair that is much weaker than the primary vortex. This is significant to the discovery, in the present work, of the '$2P_O$' mode.

Several previous controlled-vibration studies exist in the literature. Bishop & Hassan (1964), Mercier (1973), Sarpkaya (1977) and Carberry, Sheridan & Rockwell (2001, 2005) measured the fluid forcing on a vibrating cylinder, over a range of frequencies and at selected fixed values of amplitude (which we shall call 'amplitude cuts'). A significant result from these prior studies (see in particular the early work of Bishop & Hassan 1964) is the existence of a distinct jump in the phase and magnitude of the lift force as the frequency is increased through the natural vortex-shedding frequency for a stationary cylinder. In their controlled-vibration studies, Carberry *et al.* (2001, 2005) have shown that this jump is associated with a change from a 'low-frequency wake state' (equivalent to the 2P mode) to a 'high-frequency wake state' (equivalent to the 2S mode). This confirms the free-vibration studies of Brika & Laneville (1993) and Govardhan & Williamson (2000) and the earlier suggestion of Williamson & Roshko (1988) that these jumps correspond to a change from the 2P mode to the 2S mode, or vice versa. Carberry, Sheridan & Rockwell (2003) have also identified an 'intermediate wake state', equivalent to the upper-branch 2P mode found by Govardhan & Williamson (2000).

Contour plots of lift force have been generated by Staubli (1983), from his controlled-vibration experiments, and he used these contours to make predictions of the response of a free-vibration system that he compared with the free-vibration measurements of Feng (1968), at high mass damping. The prediction was reasonable for lower values of the normalized velocity (in what we call the initial branch), but such comparison was not close for higher U^* (the lower branch). The most extensive previous force-contour measurements come from experiments conducted in the MIT Towing Tank facility, presented in Gopalkrishnan (1993) and in Hover, Techet & Triantafyllou (1998). They compiled force coefficients in phase with velocity ($C_Y \sin\phi$) and in phase with acceleration ($C_Y \cos\phi$), over a wide range of normalized amplitude and wavelength. Hover *et al.* (1998) were also able to run ingenious virtual free-vibration experiments in the same facility, using their 'virtual cable testing apparatus'. Their zero-fluid-excitation contour ($C_Y \sin\phi = 0$) yielded reasonable agreement with one of their (virtual) free-vibration responses, at very low mass damping. However, some portions of the free-vibration response were situated in regions in which the force contours from controlled vibration predicted negative excitation.

Two recent numerical studies (by Leontini and co-workers at Monash University and Willden and co-workers at Imperial College) have investigated the modes of vortex formation and contours of energy transfer for low Reynolds numbers, $Re = 50$–300. In the first study, Leontini *et al.* (2006*b*) employed two-dimensional numerical simulations and found no discernible change of vortex wake mode as the energy transfer (from fluid to body motion) changed sign from negative to positive. Interestingly, they found that the $P + S$ vortex wake mode could exhibit a small regime of positive excitation. The complex picture of energy-transfer contours and modes is also influenced by the Reynolds number. In a separate paper, Leontini *et al.* (2006*a*) noted that experimental work had been unable to capture all the characteristics of vortex-induced vibration, especially the energy transfer. Numerical predictions of response, based on a driven vibration study, were close to simulated

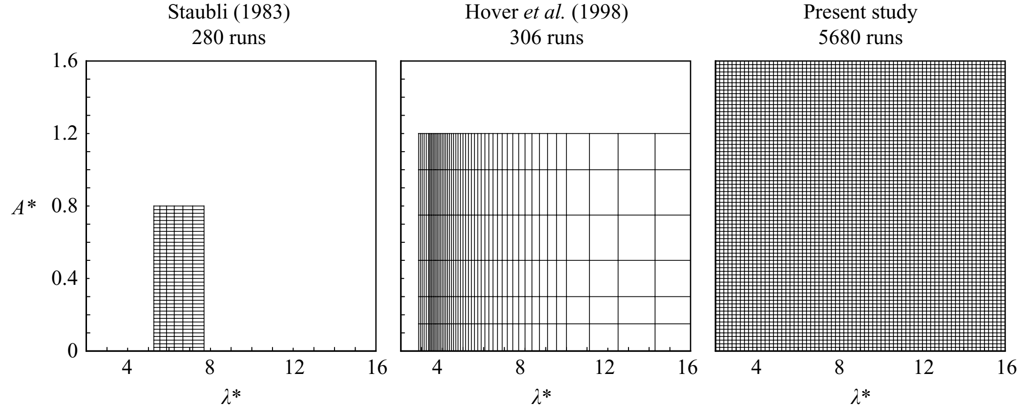

FIGURE 1. Grid resolution of controlled-vibration measurements from previous studies and in the present study. We are able to obtain a very high resolution, as well as a wide range of the parameters.

free-vibration response for the Reynolds number of 200, in the two-dimensional laminar vortex-formation regime. In the second study, Willden, McSherry & Graham (2007) reported an ongoing study at $Re = 100$ and 300, which so far has shown that the zero-energy-transfer conditions correspond closely with the amplitude-response plots of low damped experiments and simulations. They have employed two-dimensional and three-dimensional computations to determine conditions at which different vortex wake modes occur.

One important question, mentioned earlier, is to what extent can measurements from controlled vibration be applied to the case of a freely vibrating, elastically mounted cylinder? Carberry *et al.* (2004), using constant-amplitude experiments, compared forces and wake modes found for controlled vibration and for free vibration, finding some similar wake modes and jumps in the force and its phase. However, they also measured regimes of negative excitation from controlled vibration (suggesting that free vibration should not occur) under conditions at which free vibration has been readily found. They concluded that sinusoidal controlled motion ‘does not simulate all the key components of the flow-induced motion’. This seems reasonable based on the results that were available at the time from different facilities or groups. However, Morse & Williamson (2006) made direct comparisons between free and controlled vibrations and showed that if the experimental conditions are matched, controlled vibration can yield fluid forces which are in very close agreement with results from free vibration, over an entire response plot. It is possible that this careful matching of conditions is a key point in these studies. In this paper, we shall present further amplitude-response predictions, using our controlled-vibration force contours, which are in close agreement with measured free-vibration response, at both high and low mass damping. This indicates that the use of controlled vibration is indeed quite reasonable to predict free-vibration response.

In this work, we measure the fluid forcing for a cylinder oscillating under controlled vibration over an extensive range of normalized amplitude and wavelength, with much higher resolution than in previous data sets, as indicated by figure 1. The use of almost 6000 runs leads to sufficiently fine resolution to allow a study of distinct fluid-forcing regimes, some of which overlap and lead to phenomena we shall discuss later in § 6. Over this wide regime of amplitude and wavelength, we present selected examples of the vorticity dynamics associated with certain vortex modes in the wake, using digital particle image velocimetry (DPIV) measurements. The force measurements are used to predict the behaviour of a freely vibrating cylinder and to explain the mode transitions which occur between different branches of response.

Following a description of the experimental details in § 2, we introduce a set of regimes of vortex formation in § 3, which we have been able to identify from the fluid-forcing measurements. In particular, in this section, we present the overlap regime associated with the $2\mathrm{P}_O$ vortex-formation mode, which is significant because this mode is responsible for yielding a positive excitation at the highest amplitude and so would be associated with the peak-amplitude response in free vibration. In § 4, we present contours of the fluid forcing obtained from our high-resolution data and explore the relationship between the fluid excitation and the vortex-formation mode, particularly for our comparison between the $2\mathrm{P}_O$ and 2P modes. In an earlier short paper (Morse & Williamson 2009*a*) we have presented selected force-contour plots, as found here, but we have included several other such plots in a more complete set, for reference $\{C_Y, \phi, C_Y \sin\phi, C_Y \cos\phi, C_{vortex}, \phi_{vortex}\}$. The last two parameters refer to 'vortex-force' magnitude and phase. Also, in this earlier publication, we have studied the force time traces and force spectra as one moves across various boundaries of the fluid-force regimes to further characterize such regimes.

In § 5 of this paper, we use our force contours to accurately predict the response of a freely vibrating cylinder, demonstrating good agreement between prediction and direct free-vibration measurements. The introduction of energy portraits in § 6, illustrating the excitation energy and energy dissipated by damping, as a function of amplitude, enables us to further understand the existence of hysteresis between modes of vibration, as well as intermittent switching between modes. The energy portraits enable us to illustrate clearly the stability and instability of equilibrium amplitude solutions, predicted from the force-contour data. In § 7, employing the finely resolved force contours, we have been able to identify the regime within the amplitude–wavelength plane for which free vibration is possible, taking into account stability of the possible vibration solutions. This is followed by our conclusions in § 8.

2. Experimental details

The present experiments were conducted in the Cornell-ONR Water Channel, which has a cross-section 38.1 cm wide and 50.8 cm deep. The turbulence level in the test section of the water channel is less than 0.9 %. We match very closely the experimental arrangement used in the free-vibration study of Govardhan & Williamson (2000) with our controlled-vibration arrangement here. In both cases a circular cylinder is suspended vertically in the water channel and oscillated transverse to an incoming flow, as shown schematically in figure 2. The only difference is that in the free-vibration case, the cylinder is attached to a spring-mounted carriage running on air bearings, which oscillates freely, transverse to the flow, due to vortex-induced motion. In the controlled-vibration case, the cylinder is mounted on a transverse lead screw attached to a computer-controlled motor, and it oscillates with a prescribed sinusoidal motion.

We use a test cylinder of diameter 3.81 cm and submerged length 38.1 cm with the flow speed kept constant to give a Reynolds number $Re = 4000$. In the appendix, we also show results for $Re = 12\,000$, obtained using a larger cylinder of diameter 6 cm and length 42 cm with a higher flow velocity. A fixed end plate is placed 2 mm

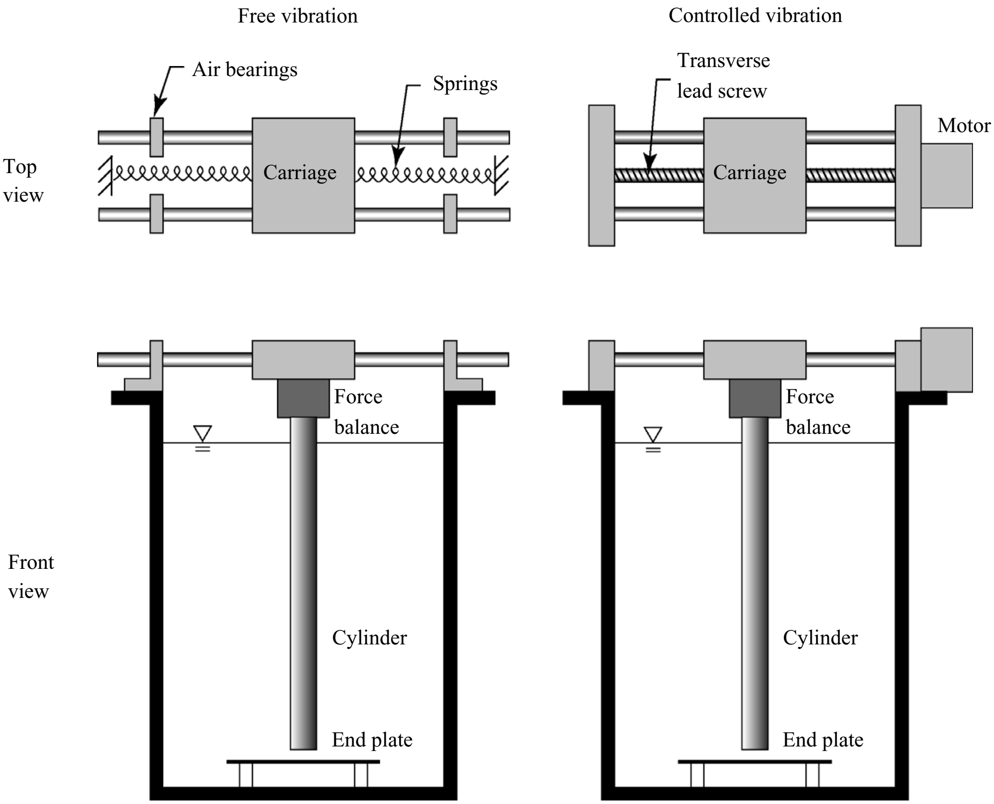

FIGURE 2. Schematic diagram of the experimental arrangement which is closely matched to the arrangement for free vibration. In both cases the cylinder is suspended vertically in a water channel and oscillates transverse to the flow (into the page). For the controlled-vibration case we prescribe the motion using a computer-controlled motor and lead screw.

below the bottom of the cylinder (but not in contact with the cylinder) to encourage two-dimensional vortex shedding, following the study of Khalak & Williamson (1996). For each Reynolds number, we carry out a total of 5680 runs, each for 100 cycles of oscillation, to yield a total of approximately 1000 h worth of data. Normalized amplitude (A^*) is varied from 0.02 to 1.6, with a resolution of 0.02. Normalized wavelength (λ^*) is varied from 2 to 16, with a resolution of 0.2. Such an extensive data set is only possible because the experiment is conducted in a continuously flowing water channel facility, rather than a towing tank facility, and thus can be automated to run unattended for a large number of experimental runs, often overnight.

A two-axis force balance utilizing linear variable differential transducers (LVDTs) is used to measure the lift and drag forces on the cylinder. The transverse displacement of the cylinder is measured using a non-contact (magnetostrictive) position transducer. For each run, the fluid-force magnitude (F_1) and phase angle (ϕ) at the fundamental (body-oscillation) frequency are calculated using a Fourier-series analysis. Relevant fluid-forcing quantities, such as $C_Y \sin\phi$ and C_{EA}, are obtained using just the force component at the body-oscillation frequency. In most cases, the fluid forcing is quite sinusoidal and thus represents essentially all of the force signal content. In particular, the fluid forcing is less sinusoidal in the coalescing 2S mode, or the C(2S) mode, regime and desynchronized wake regime, as might be expected. This is expanded upon in Morse & Williamson (2009*a*).

In addition to the extensive force measurements described above, we use DPIV to measure vorticity in the wake of the vibrating cylinder, for the case of $Re = 4000$. The flow is seeded with 14 μm silver-coated glass spheres, which are illuminated by a sheet of laser light from a 50 mJ Nd:Yag pulsed laser. Pairs of particle images are acquired using a Jai CV-M2CL CCD camera (1600×1200 pixels) and analysed using cross-correlation of sub-images. We use a two-step windowing process (with window shifting) to obtain particle displacements between image pairs. Further details on our DPIV processing may be found in Govardhan & Williamson (2000). The viewing area is 26×34 cm^2, corresponding to 6.75×9 diameters. The time between images is adjusted to vary between 10 and 20 ms depending on the cylinder-oscillation parameters. Vorticity fields calculated from the image pairs are phase averaged over approximately 10–20 cycles to remove the small weak-vorticity structures generated by intermittent small-scale three-dimensionality in the flow and thus obtain a clear picture of the dynamics of the principal spanwise vorticity.

3. Regimes of fluid forcing and vortex-formation modes

Employing our controlled-vibration data, we are able to identify conditions at which the fluid forcing shows qualitative abrupt jumps, as amplitude or frequency is varied, similar to the jumps found in the ‘amplitude cuts’ of previous controlled-vibration studies. We follow these jumps throughout the normalized amplitude–wavelength plane and are able to identify clear boundaries separating regions of distinct fluid forcing, indicated by the coloured regimes in figure 3(*a*). These boundaries show a remarkable similarity to the boundaries separating different vortex-formation modes in the map of Williamson & Roshko (1988), shown in figure 3(*b*), which were identified by (fine-resolution) flow-visualization observation of the flow patterns. We naturally expect that the regions found here, based solely on the fluid forcing, will correspond with similar modes of vortex formation found by Williamson & Roshko (1988).

By measuring the wake vorticity at certain locations in the amplitude–wavelength plane, we confirm the existence of certain modes of vortex formation that are labelled for each fluid-forcing regime in figure 3. The P+S, 2S and 2P modes are presented in figures 4(*a*)–4(*c*). The 2S and 2P modes may be compared with such vortex modes from free vibration in Govardhan & Williamson (2000). Added to these classical modes, we have been able to identify a distinct new mode of vortex formation ($2\mathrm{P}_O$ mode), existing in its own clearly defined region of the amplitude–wavelength plane, overlapping the boundary between the 2S and 2P regions. Vorticity measurements of this mode reveal that although there are two pairs of vortices shed per cycle of vibration, the secondary vortex in each pair is much weaker than the primary vortex and decays rapidly as the vortex pair moves downstream, as shown in figure 4(*d*). This is in contrast with the classical 2P mode in figure 4(*c*), where the primary and secondary vortices in a vortex pair have roughly equal strength (Govardhan & Williamson 2000). We label this new mode as ‘$2\mathrm{P}_{OVERLAP}$’ or simply ‘$2\mathrm{P}_O$’. We find significant overlapping regimes, in figure 3, where the wake can switch intermittently between the $2\mathrm{P}_O$ and 2P modes (or between the $2\mathrm{P}_O$ and 2S modes), even if the cylinder is vibrating with steady amplitude and frequency.

The identification of this distinct $2\mathrm{P}_O$ mode allows us to clarify the vortex-formation mode for the upper and lower branches in a free-vibration response. Our initial interpretation of the results of Govardhan & Williamson (2000) was that the 2P mode they found for the upper branch of response, which exhibited a much smaller secondary vortex (as for the $2\mathrm{P}_O$ mode), was the same mode essentially as the 2P mode in the lower-amplitude branch but was simply affected in its configuration

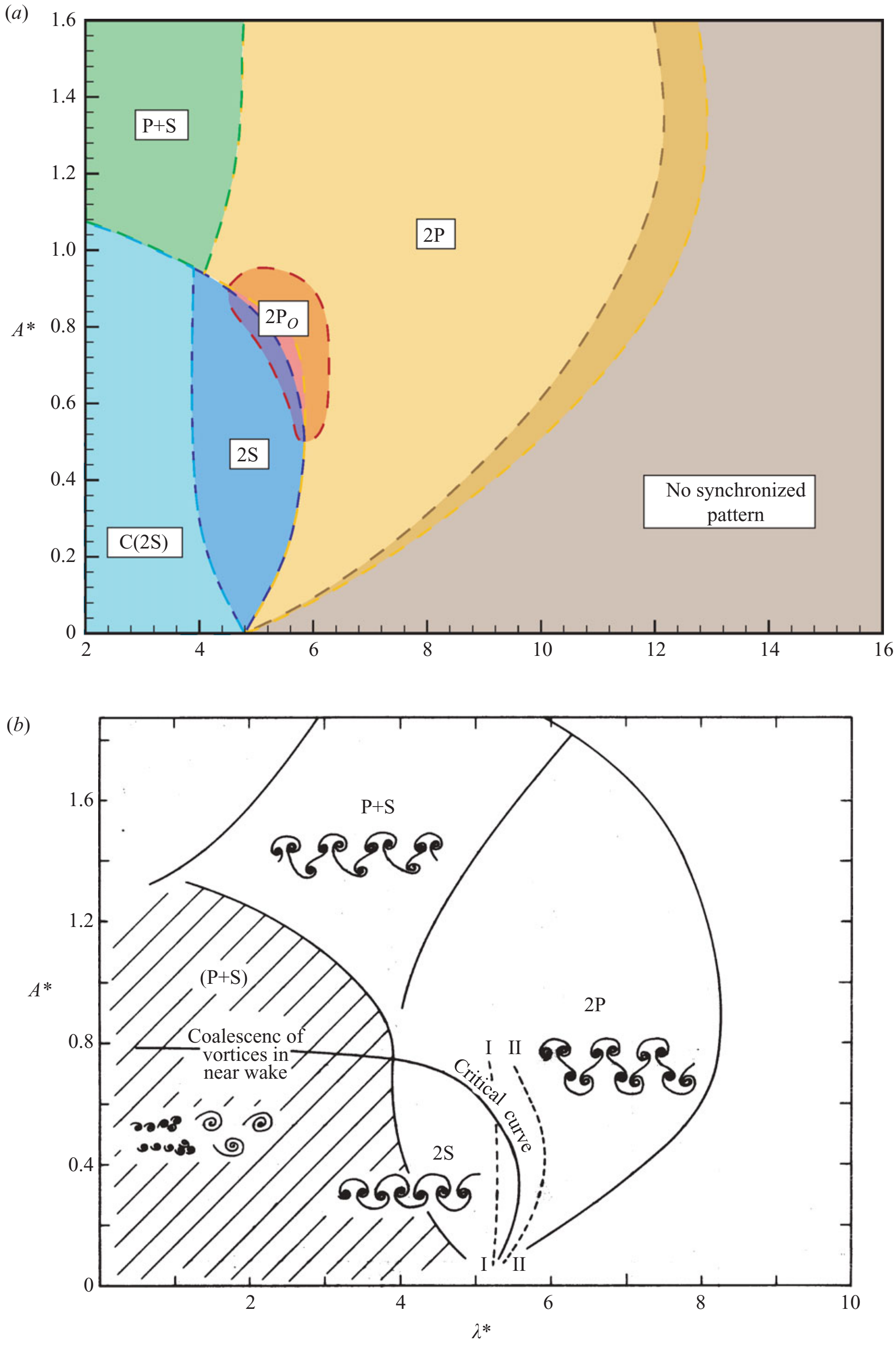

FIGURE 3. Map of vortex-shedding regimes. There is a remarkable similarity between the mode boundaries we have identified in the present study from force measurements in (*a*) and the boundaries identified by Williamson & Roshko (1988) from flow visualization in (*b*). Overlapping colours indicate regions in which two vortex-shedding modes overlap.

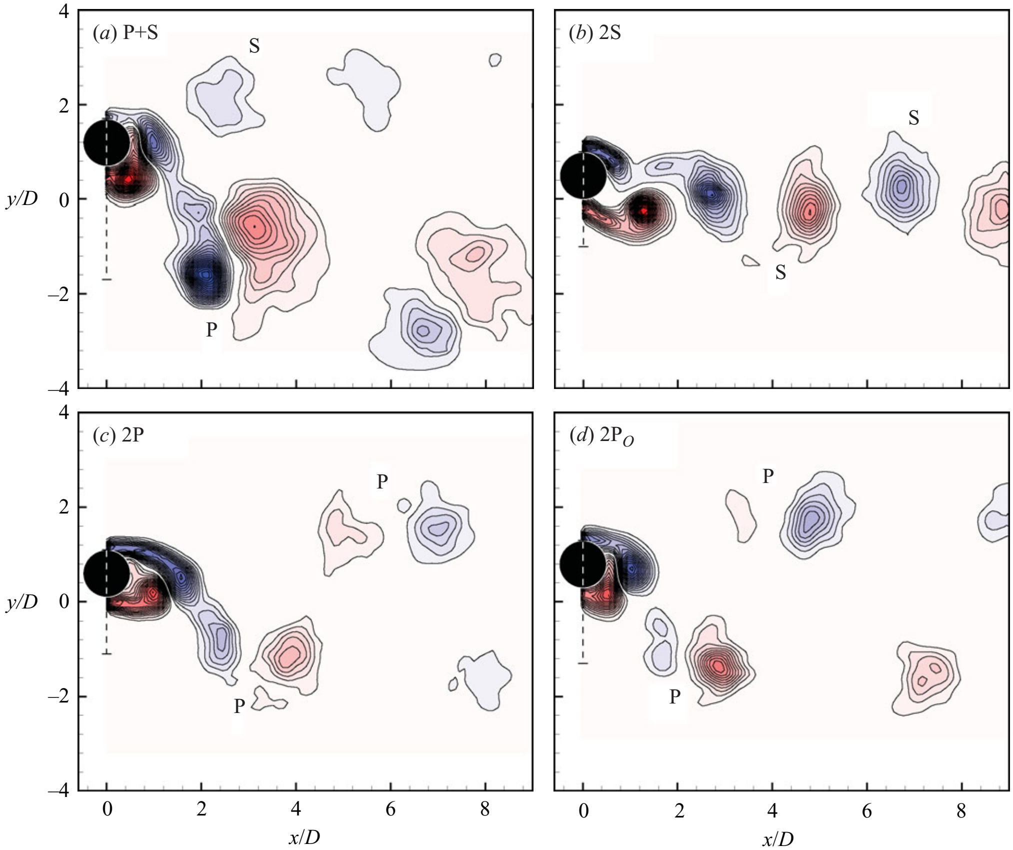

FIGURE 4. Vorticity fields for each of the main vortex-shedding modes {P + S, 2S, 2P, 2P$_O$}. We observe a switch in timing of the initially shed vortex from the 2S mode to the 2P mode. In all cases the vorticity field is phase averaged over 20 cycles of oscillation; contour levels shown are $\omega D/U = \pm 0.4, \pm 0.8, \pm 1.2, \ldots$. Measurement locations in the amplitude–wavelength plane are as follows: P + S mode, ($A^* = 1.2$, $\lambda^* = 4.0$); 2S mode, ($A^* = 0.5$, $\lambda^* = 5.0$); 2P mode, ($A^* = 0.6$, $\lambda^* = 6.4$); 2P$_O$ mode, ($A^* = 0.8$, $\lambda^* = 5.6$).

by an increase in amplitude. The present work clearly shows that the existence of the 2P$_O$ mode is not simply an amplitude effect, but instead it is a mode that is quite distinct from the 2P mode, existing at the same amplitude and wavelength. The concept of an overlap region could not be discovered from free vibration, because the 2P and 2P$_O$ modes yield different values of the fluid excitation and thus cannot sustain free vibration at the same amplitude level. This is further discussed in § 6.

In addition to the principal four modes of vortex formation shown in figure 4, namely the set {2S, 2P, 2P$_O$, P+S}, we also find a region in which the wake is not synchronized with the cylinder oscillation, at high normalized wavelength (the brown shaded region in figure 3), and a region in which a 2S mode initially forms behind the cylinder, but the vortices coalesce downstream, at low normalized wavelength, called the C(2S) mode in figure 3. Finally, there is a small band in which the desynchronized wake region overlaps with the 2P mode, in which the wake will switch intermittently between these two conditions. The desynchronized wake mode, and the C(2S) mode, are characterized using detailed force time traces and spectra in Morse & Williamson (2009*a*).

In this study, the existence of an overlapping mode is significant because it is associated with the maximum amplitude at which one experiences positive excitation. It will thus be the mode yielding the peak resonant amplitude in free vibration. We shall also see that as a result of the fact that the $2P_O$ mode overlaps other regimes, the possible mode jumps and interplay between the modes can become quite complex, and this will be investigated in § 6.

4. Contours of fluid excitation and effective added mass

Although we may present several useful fluid-forcing quantities in a set of contour plots, we choose in this paper to focus on the two most relevant quantities for the prediction of free-vibration responses, namely the fluid excitation ($C_Y \sin\phi$) shown in figure 5 and the effective added-mass coefficient (C_{EA}) shown in figure 6. The fluid excitation primarily affects the amplitude of vibration (A^*), as shown in the amplitude equation (1.4) above. On the other hand, the effective added mass (C_{EA}) affects primarily the frequency of vibration (f^*), as shown in the frequency equation (1.5), and will be of use in predicting response in § 5. We also include here a related plot in figure 7, in the amplitude–wavelength plane, of lines for which the normalized velocity (U^*) is a constant. We shall use this plot extensively in § 6 to show how the energy transfer into the body motion varies as a function of amplitude, for fixed values of the normalized velocity, U^*.

The regions of positive fluid excitation (which is necessary for free vibration to occur) exist within the 2S, 2P, $2P_O$ and desynchronized regimes that are shown in figure 5. In fact, it is significant that the highest amplitude for which there is positive fluid excitation lies in a $2P_O$ overlap region. In this region, the wake may intermittently switch between a $2P_O$ mode of vortex shedding, which will yield a net positive excitation, and a 2P mode of vortex shedding, which will yield a net negative excitation, as shown in the time trace of the instantaneous rate of energy transfer (i.e. power) in figure 8. This means that for the conditions shown in figure 8 ($A^* = 0.8$, $\lambda^* = 5.4$), free vibration could occur only if the mode of vortex formation is $2P_O$. If the mode of vortex formation were to switch to the 2P mode, the fluid excitation would become negative, and the amplitude would drop until the fluid excitation becomes positive for this 2P mode (A^* below about 0.56) or until the vortex formation possibly switches back to the $2P_O$ mode. This switching of vortex-formation modes is what leads to the intermittent switching between the upper branches and lower branches of a free-vibration response, as explained in more detail in § 6.

In order to better understand the difference between the $2P_O$ and 2P vortex-formation modes, we shall briefly introduce the concept of a 'vortex force'. Following the analysis of Lighthill (1986) and Govardhan & Williamson (2000), we decompose the total transverse fluid-force coefficient (C_{TOT}) into a 'potential-force' component (C_{POT}), given by the potential added-mass force, and a 'vortex-force' component (C_{VORT}), due to the dynamics of vorticity. For sinusoidal body motion, the potential-force coefficient can be calculated to be

$$C_{POT}(t) = 2\pi^3 \frac{y(t)/D}{(U^*/f^*)^2}. \tag{4.1}$$

Thus we see that the instantaneous potential added-mass force C_{POT} is always in phase with the cylinder motion, $y(t)$, as one might expect. The vortex-force coefficient

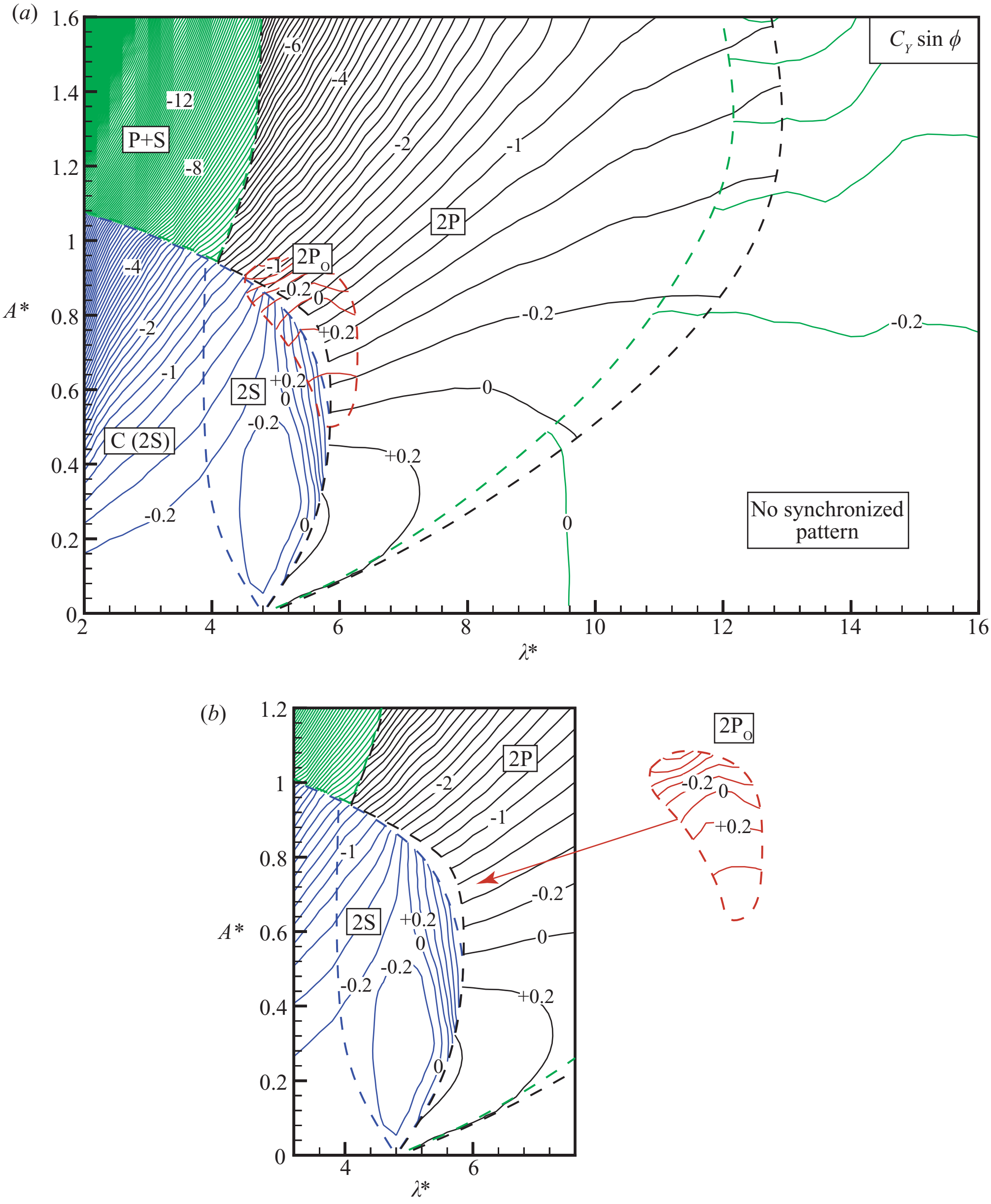

FIGURE 5. Contours of the force in phase with velocity, $C_Y \sin\phi$ (normalized 'fluid excitation'), for $Re = 4000$. Boundaries between modes are indicated by the dashed lines. Note that contours overlap in regions in which multiple vortex-shedding modes are possible. In (*b*) we pull away the $2P_O$ mode to more clearly show the 2P and 2S mode regions underneath. Contour interval is 0.2.

can then be found by subtracting the potential-force coefficient from the total force coefficient:

$$C_{VORT}(t) = C_{TOT}(t) - C_{POT}(t). \tag{4.2}$$

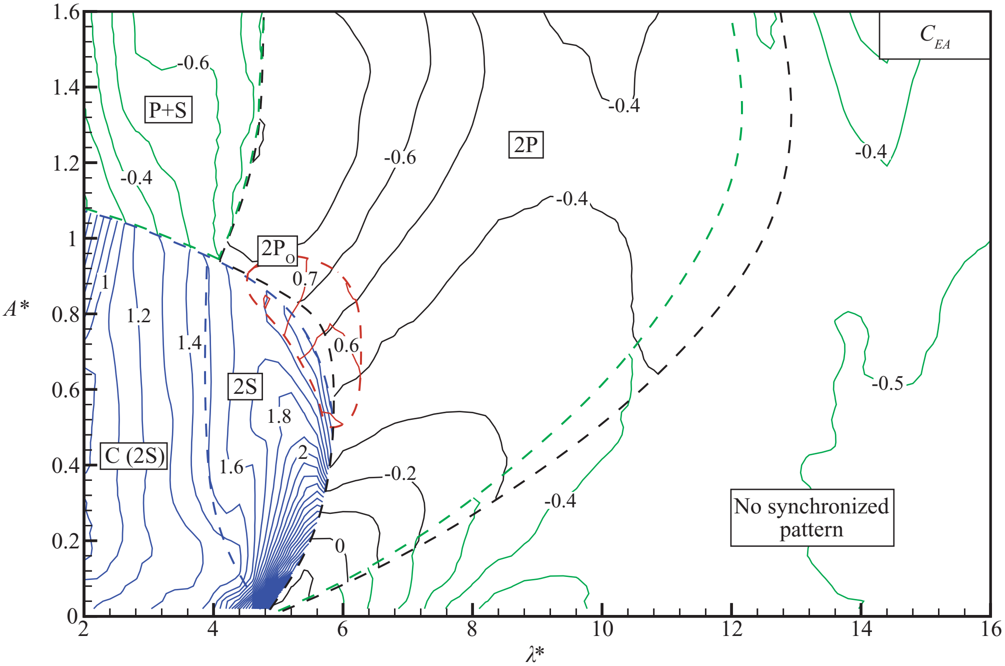

FIGURE 6. Contours of the effective added mass, C_{EA}, for $Re = 4000$. Boundaries between modes are indicated by the dashed lines. Note that contours overlap in regions in which multiple vortex-shedding modes are possible. Contour interval is 0.1.

So that we may further illustrate the difference between the $2P_O$ and 2P vortex modes, we show force time traces and wake-vorticity fields for each mode, taken during a single experimental run, shown in figure 9. The timing of vortex shedding is quite similar for the two cases even though the $2P_O$ mode shows a much weaker secondary vortex. Thus the phase of the vortex force (see time trace for C_{VORT} in figure 9) is similar for the two cases; however, the magnitude of the vortex force is much lower for the $2P_O$ mode than for the 2P mode. Therefore, when we superpose the potential force (which will be the same for both modes since the motion is the same) on to the vortex force to yield the total force (C_{TOT}), we find almost a 180° switch in phase angle for the $2P_O$ mode. The $2P_O$ mode then delivers a positive energy transfer into the body motion, while the 2P mode generates negative energy transfer.

For high amplitudes ($A^* = 0.80$), as in the example above, the 2P mode of vortex formation yields negative excitation and thus cannot sustain free vibration. However, at amplitudes below about 0.6, the fluid excitation for the 2P mode becomes positive. One might ask how the wake vortex dynamics change to accomplish this? As the transverse amplitude is decreased within the 2P region, the wake becomes narrower, as shown in figure 10. In addition, the timing of vortex shedding shifts slightly. Even this small change in timing, as the amplitude (A^*) falls below 0.6, is sufficient to alter the vortex phase to cause a switch from negative excitation to positive excitation; in essence, there is no dramatic change in the vortex-formation pattern, as energy transfer becomes positive.

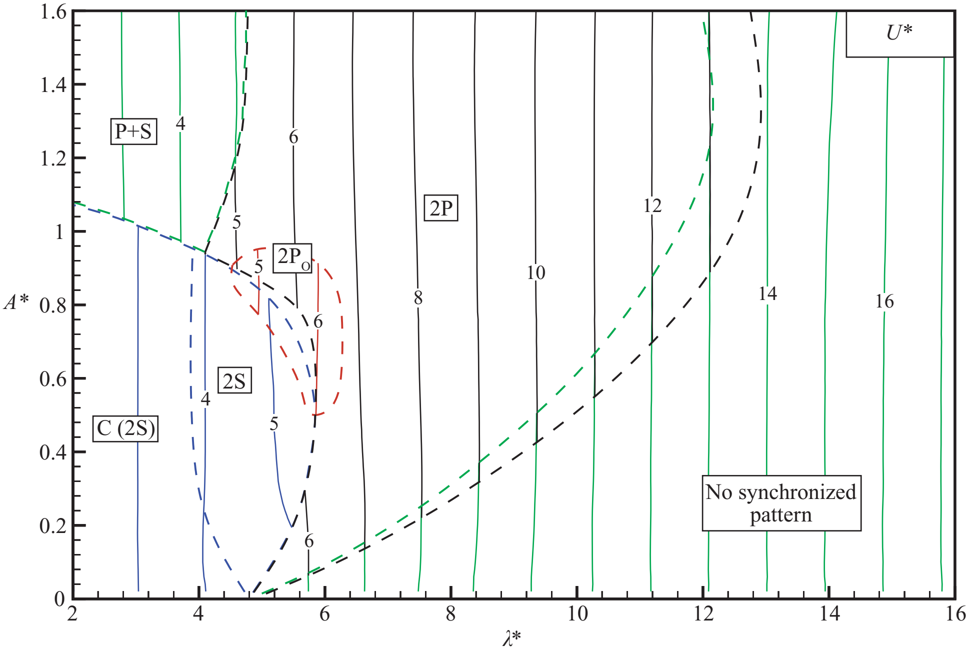

FIGURE 7. Cuts of constant normalized velocity (U^*) for $Re = 4000$ and $m^* = 10.0$; U^* cuts are determined from the frequency equation (1.5) using contours of C_{EA}. Note that cuts are discontinuous across vortex-formation-mode boundaries.

5. Prediction of a free-vibration response

The availability of our high-resolution force contours now enables us to predict the response of a freely vibrating cylinder, using (1.4) and (1.5). We are required to set the system parameters $\{m^*, \zeta, U^*\}$ and then to solve for the response parameters $\{A^*, f^*\}$. We have measured the fluid-forcing quantities $\{C_Y \sin\phi, C_{EA}\}$ as functions of A^* and λ^* or equivalently as a function of A^* and f^*, if one fixes the normalized velocity, U^*. Thus we can simply solve numerically for amplitude (A^*) and frequency (f^*) and build up an entire response plot at a given m^* and ζ as one varies U^*.

A simpler way to understand this process is to combine the frequency equation (1.5) and the amplitude equation (1.4), to give an equation with only the combined mass damping on the left-hand side:

$$(m^* + C_A)\zeta = \frac{C_Y \sin\phi}{4\pi^3 A^*}\lambda^{*2}\sqrt{\frac{m^* + C_A}{m^* + C_{EA}}}, \tag{5.1}$$

where we have also used $U^*/f^* = \lambda^*$. Now, for a given mass ratio, we can plot contours of the conglomeration of non-dimensional variables on the right-hand side of (5.1). Each contour will then represent a predicted free-vibration response at a particular value of the combined mass damping, $(m^* + C_A)\zeta$. The solution for a system at zero damping will always follow the zero-excitation contour of $C_Y \sin\phi = 0$. (Note that for a high enough mass ratio, the frequency ratio, f^*, will be close to 1, and contours of C_{EA} are not actually needed.) It is important to note that for reasonable comparisons between predictions and free-vibration experiments, we make

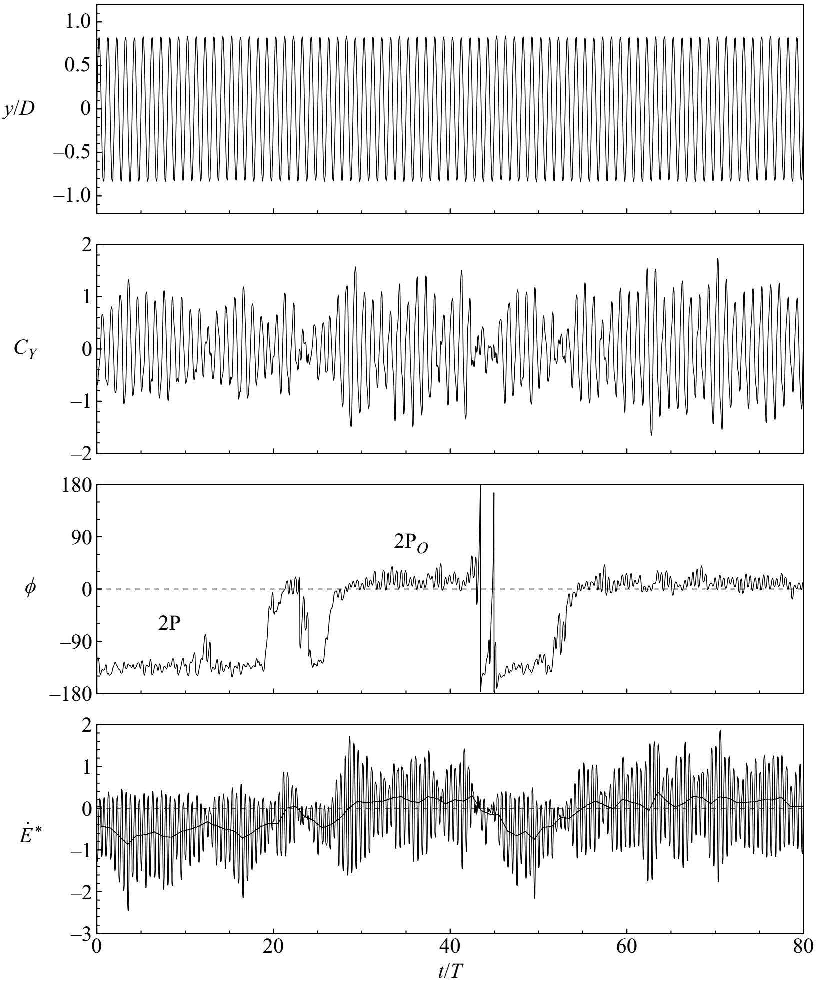

FIGURE 8. Force and energy-transfer time traces in the $2P_O$–2P overlap region ($A^* = 0.80$, $\lambda^* = 5.6$). The mode switching is most apparent in the phase angle, ϕ. The instantaneous rate of energy transfer $\dot{E}^*$ has large fluctuations, but cycle averages (shown as a thicker line) show that the $2P_O$ yields a net positive fluid excitation, while the 2P mode yields negative excitation.

the assumption that damping and stiffness are linear and may be accurately measured for the free-vibration case. Indeed, in the work of Govardhan & Williamson (2006) and in several previous papers from the same laboratory, using the same facility, this was checked thoroughly. The air-bearing damping was very small throughout the experiments conducted in free vibration; the linearity of the damping in a particular measurement was indicated by the closely linear form of the logarithmic decay plots and was generally to the level of 1 % nonlinear. The spring stiffness was very linear, with nonlinearities amounting to less than 1 % of the stiffness.

With this approach, we are readily able to use our controlled-vibration data to predict the response of a freely vibrating cylinder, in the examples of figure 11. We find close agreement with measured free-vibration amplitude response (taken from Govardhan & Williamson 2006), for both high and low mass damping. To obtain the complete predicted response plot, we look for solutions in each of the fluid-forcing

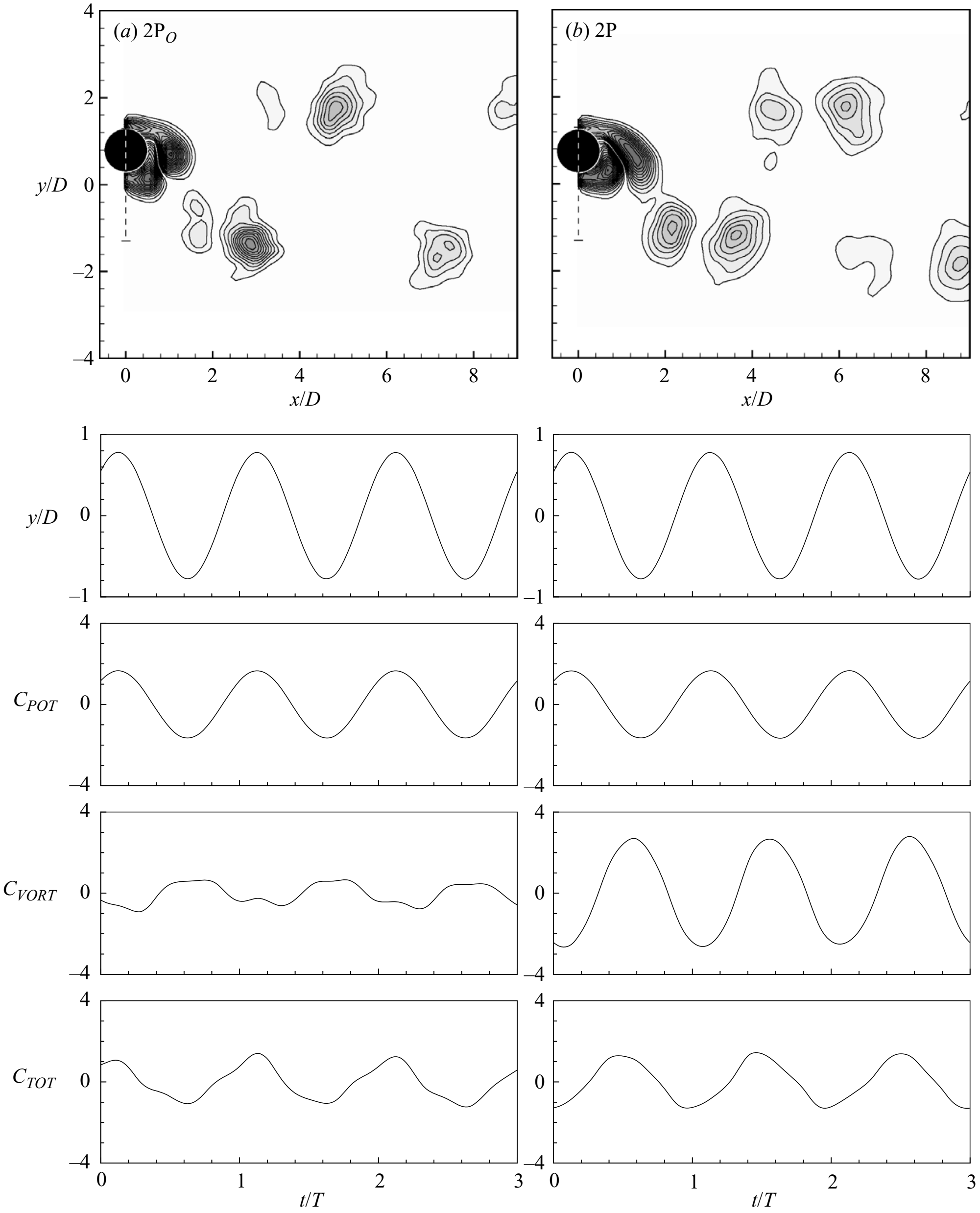

FIGURE 9. Vorticity fields (top panel) and decomposed force time traces (lower panels) in the $2P_O$–2P overlap region, for the same location as in figure 8 ($A^* = 0.80$, $\lambda^* = 5.6$). The vorticity field shows a similar timing in vortex shedding but with a much weaker secondary-vortex strength in the $2P_O$ case. The smaller magnitude of the vortex force in the $2P_O$ case leads to a switch in phase of the total force. Vorticity contour levels shown are $\omega D/U = \pm 0.4, \pm 0.8, \pm 1.2, \ldots$.

regimes identified in figures 5 and 6. For the low-mass-damping case, where we find a three-branch response, the initial branch lies in the 2S region, the upper branch in the $2P_O$ region and the lower branch in the 2P region. For the high-mass-damping case, there are two branches: an initial branch in the 2S region and a lower branch in

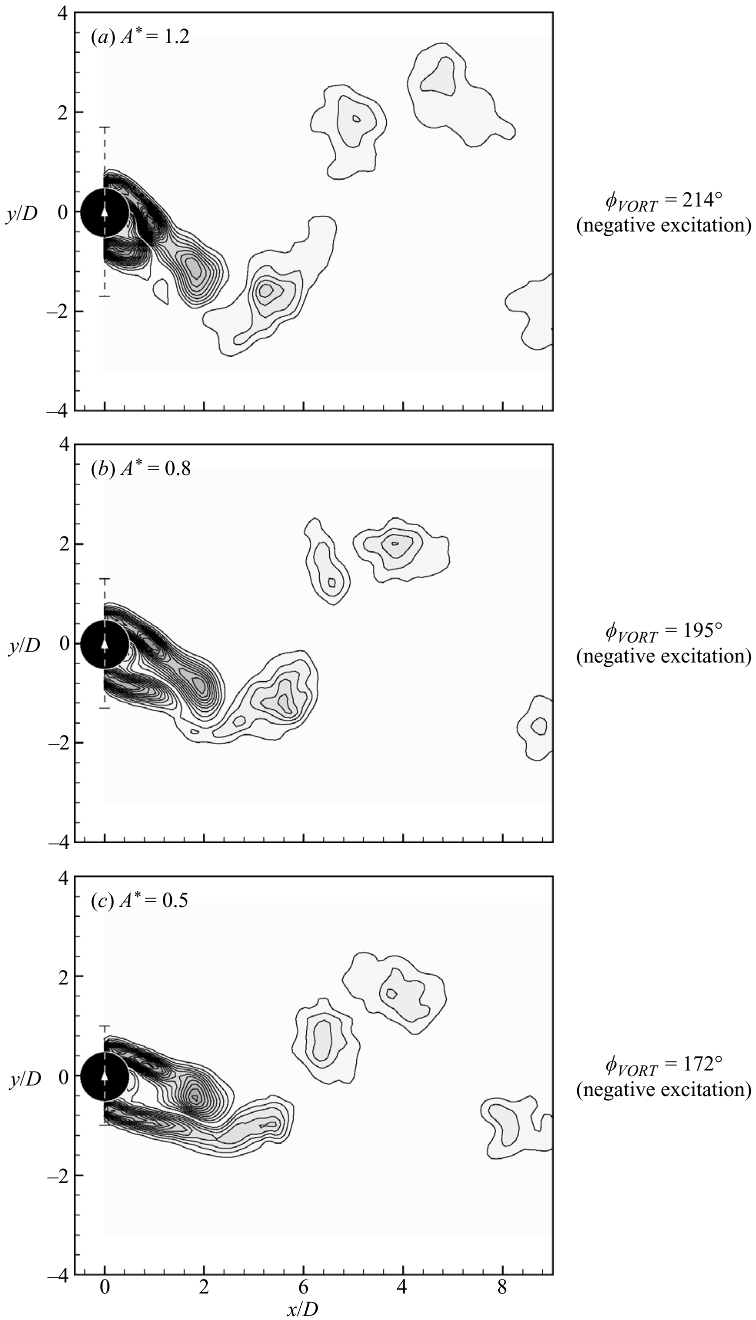

FIGURE 10. Vorticity fields for decreasing amplitude in the 2P region ($\lambda^* = 8.0$). The vortex-formation mode does not change; however the timing of vortex shedding becomes slightly later as amplitude decreases, causing a switch from negative excitation to positive excitation. Vorticity contour levels shown are $\omega D/U = \pm 0.4, \pm 0.8, \pm 1.2, \ldots$.

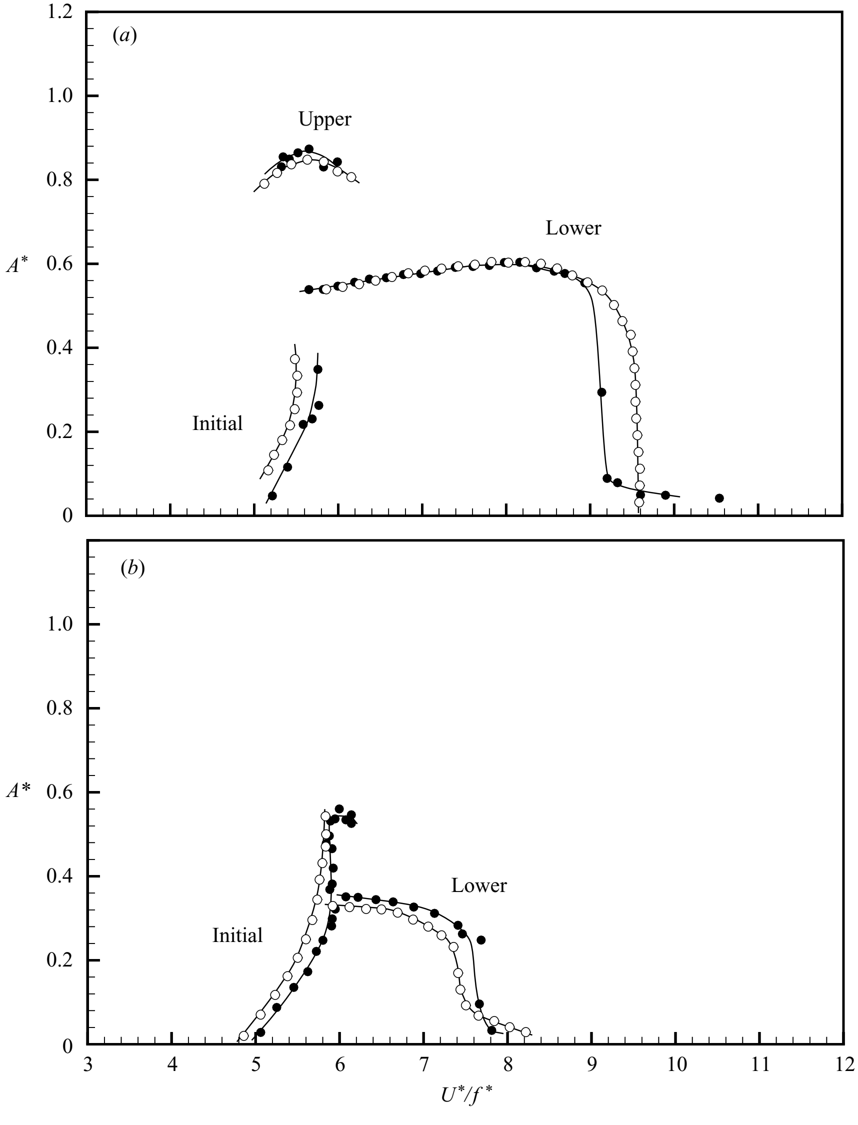

FIGURE 11. Measured and predicted amplitude response for a free-vibration system at (*a*) low mass damping, $(m^* + C_A)\zeta = 0$, and (*b*) high mass damping, $(m^* + C_A)\zeta = 0.340$: ●, measured free-vibration response from Govardhan & Williamson (2006); ○, predicted response from the present controlled-vibration data. In both cases $m^* = 10.49$; $Re = 4000$ for the controlled-vibration case; $Re = 4000$ at peak amplitude for the free-vibration case.

the 2P region. The 2S–2P$_O$ and 2P$_O$–2P overlap regions can lead to some interesting behaviour as we discuss later in § 6.

The agreement between predicted and measured free-vibration responses shown here is much closer than has been found in previous studies and is only possible because of the high resolution of our force data and the careful matching of the experimental arrangement between the controlled and free-vibration cases. The Reynolds number at peak response was also matched to be equal to 4000 for the two cases (noting that for the controlled-vibration prediction, $Re = 4000$ throughout the response plot). This match of the Reynolds number is important because the peak amplitude in the upper branch depends on *Re*, as explained in Govardhan & Williamson (2006) and discussed briefly below.

In addition to the fluid-force contours at $Re = 4000$, we have generated complete contour plots at $Re = 12\,000$ and show for brevity only one of these plots (for the excitation energy, $C_Y \sin\phi$), within the appendix. We have been able to predict complete curves of peak amplitude versus mass damping from the two Reynolds numbers, using the idea of the 'modified Griffin plot' put forward in Govardhan & Williamson (2006). The agreement with the predictions from the controlled-vibration contour plots with the free-vibration data is good. We are also able to search for the peak amplitude A^*_{PEAK} which is found when one has zero damping, taken from the point at which the curve for zero excitation energy ($C_Y \sin\phi = 0$) reaches a maximum for each Reynolds number. A comparison of this predicted peak amplitude, A^*_{PEAK}, with the extensive compilation of peak amplitude from free-vibration data shows good agreement.

6. Introducing 'energy portraits' to understand mode transitions

In the previous section we demonstrated the potential for accurate response prediction, using our contour plots of force. In this section, we study the transitions that occur between the different response branches and stability of equilibrium amplitude solutions, using the concept of an energy portrait.

6.1. *Introduction of the concept of an energy portrait*

We define an energy portrait as a plot of the energy of excitation (E^*_{IN}) and the energy dissipated to structural damping (E^*_{OUT}) as a function of amplitude (A^*) while keeping the normalized velocity (U^*) fixed. We use these energy portraits to determine the stability of equilibrium amplitude solutions and to understand the mode transitions that occur between branches in free vibration. It is relevant in this section to refer often to figure 5, where we plot normalized energy of excitation ($C_Y \sin\phi$) and where the fluid-force regimes, and shapes of the contours, are key to the energy portraits. (One should note that plots of fluid-force excitation ($C_Y \sin\phi$) as functions of amplitude were presented as early as Griffin (1980), and as noted by Bearman (1984) in his review, Griffin's plot could be used to show that the excitation, after reaching a maximum, decreased such that there was no excitation beyond an amplitude of $1.0D$–$1.5D$.) This suggested a limiting displacement for free vibrations.

To demonstrate the usefulness of the concept of the energy portraits, we exhibit one possible shape which may occur for the fluid-excitation contours in the amplitude–wavelength plane, in figure 12(*a*). This particular variation of the excitation energy would lead to an 'S-shaped' curve for E^*_{IN} in the energy portrait of figure 12(*b*). The energy lost due to damping, E^*_{OUT}, will intersect the origin and have a slope proportional to the specific value of mass damping $(m^* + C_A)\zeta$. (One may note that the precise shape of the E^*_{OUT} curve and the shape of the $U^* = \text{constant}$ line in the amplitude–wavelength plane both depend on the frequency ratio, f^*. In general, the U^* cut will be nearly vertical, in figure 12*a*, and the E^*_{OUT} curve will be nearly straight, in figure 12*b*. Both lines become straighter as one increases the mass ratio, and $f^* \sim 1.0$.) We note here, however, that for very low mass ratios (m^* order 1 and lower) the value of f^* may depart markedly from 1, and the $U^* = \text{constant}$ contours may have a more complicated shape. A detailed analysis of vortex-induced vibration prediction at these low mass ratios forms one part of a subsequent paper (Morse &

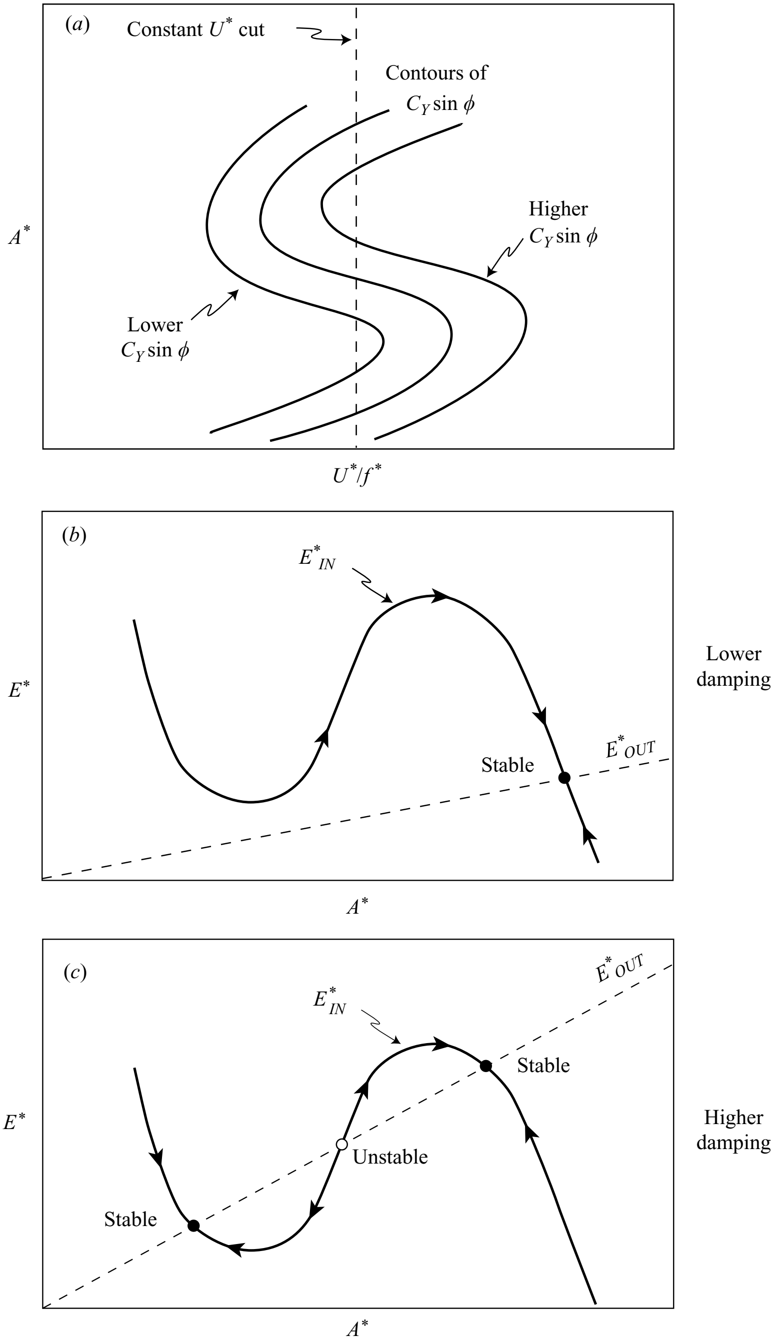

FIGURE 12. Schematic plots of an energy portrait. We (*a*) take a cut of constant normalized velocity through contours of the fluid excitation and (*b*, *c*) plot the energy balance (E^*_{IN} and E^*_{OUT}) as functions of normalized amplitude. At the equilibrium points, the energy transferred from the fluid to the cylinder is equal to the energy lost to damping. Arrows indicate direction of movement for non-equilibrium states.

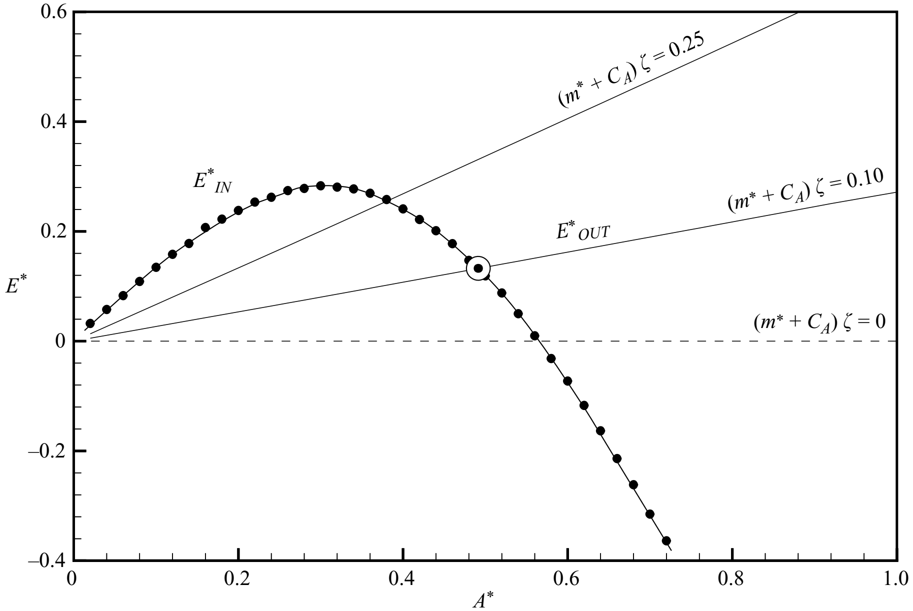

FIGURE 13. Energy portrait for $m^* = 10$, $U^* = 7.0$ (lower branch). The amplitude of the equilibrium point (⊙) decreases as the mass damping increases.

Williamson 2009*b*). In the present work, we focus on moderate-to-high mass ratios, in order to clearly present the new concepts introduced.

Steady-state response solutions are found where the energy into the system equals the energy out of the system. In our example of lower damping, in figure 12(*b*), there is one equilibrium point and hence one possible free-vibration amplitude. In our example of higher damping, in figure 12(*c*), there exist three equilibrium points, in other words three response amplitudes. However, only two of these response amplitudes are stable. The central equilibrium solution is unstable: for example if a perturbation increases the amplitude slightly, the energy into the system would be greater than the energy out of the system; the amplitude would continue to increase, ultimately reaching the upper stable solution. Stability and instability of equilibrium solutions in the energy portrait can be defined by the slope of the energy curves, at the equilibrium points, as follows:

$$\begin{aligned} &\text{stable,} \quad \mathrm{d}E^*/\mathrm{d}A^* < 0, \\ &\text{unstable,} \quad \mathrm{d}E^*/\mathrm{d}A^* > 0, \end{aligned}$$

where E^* is the net energy transfer into body motion, $E^* = E^*_{IN} - E^*_{OUT}$. Free vibration would occur at the stable-equilibrium points. In our example, there are two stable free-vibration amplitudes, which would correspond to two different solution branches in a complete response plot.

Let us now apply the concept of the energy portrait to our controlled-vibration data at $Re = 4000$. We consider a typical mass ratio for systems in water, $m^* = 10$, for which the constant U^* lines (or ‘cuts’), in the amplitude–wavelength plane, will be nearly vertical. We start with a simple case, a cut in this plane for which $U^* = 7.0$. (This cut may be seen in the amplitude–wavelength plane, in figure 7.) For our chosen values of mass damping, $(m^* + C_A)\zeta$, in figure 13, there is only one equilibrium solution

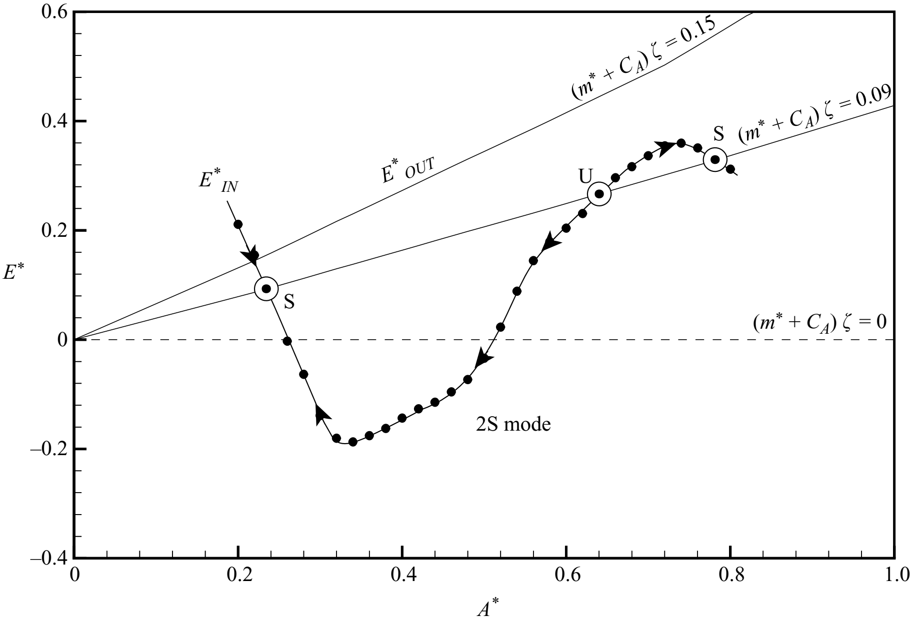

FIGURE 14. Energy portrait for $m^* = 10$, $U^* = 5.1$ (initial and upper branches). For low values of mass damping there are two stable-equilibrium points (indicated by 'S') and one unstable-equilibrium point (indicated by 'U'). The stable equilibria correspond to the initial branch and the upper branch of a free-vibration response.

(a stable solution). As the mass damping increases, the equilibrium amplitude (i.e. the predicted free-vibration amplitude) decreases. At sufficiently high mass damping, no solution will exist, in this example.

We shall now employ the energy-portrait concept in a more involved case. Let us consider a cut for which $U^* = 5.1$ in the amplitude–wavelength plane, which we expect will lead to an initial and an upper branch of free vibration. In this case, the energy into the system follows an 'S' curve, as shown in figure 14, similar to the example in figure 12, discussed above. The two stable equilibria at low and high amplitudes will correspond to the initial branch and upper branch of free vibration, respectively. Of course, the unstable equilibrium will not appear in a free-vibration response. All three solutions here represent the 2S mode of vortex formation; so this is an unusual case in which both the initial branch and the upper branch would in fact show a 2S mode of vortex formation. This unusual case has not been demonstrated in free-vibration experiments in the literature, as yet. We see from the energy portrait that under conditions of high mass damping $[(m^* + C_A)\zeta = 0.15]$, only one stable equilibrium exists, corresponding to an initial response branch in free vibration. This is consistent with experimental measurements from free-vibration results in which the upper branch disappears, for sufficiently high mass damping.

From the excitation-force contours in figure 5, we note there exists a region in which the 2S and the $2\mathrm{P}_O$ regimes overlap such that the fluid excitation will not be continuous across this transition. The cut for $U^* = 5.1$ passes through this overlap region (a similar cut, $U^* = 5.0$, can be seen in figure 7). Therefore the energy portrait will show a small range of amplitudes in which two possibilities exist for E^*_{IN}, depending on the mode of vortex shedding (2S or $2\mathrm{P}_O$). In figure 15, we now include this second branch of the excitation energy, corresponding to the 2Po mode (E^*_{OUT}

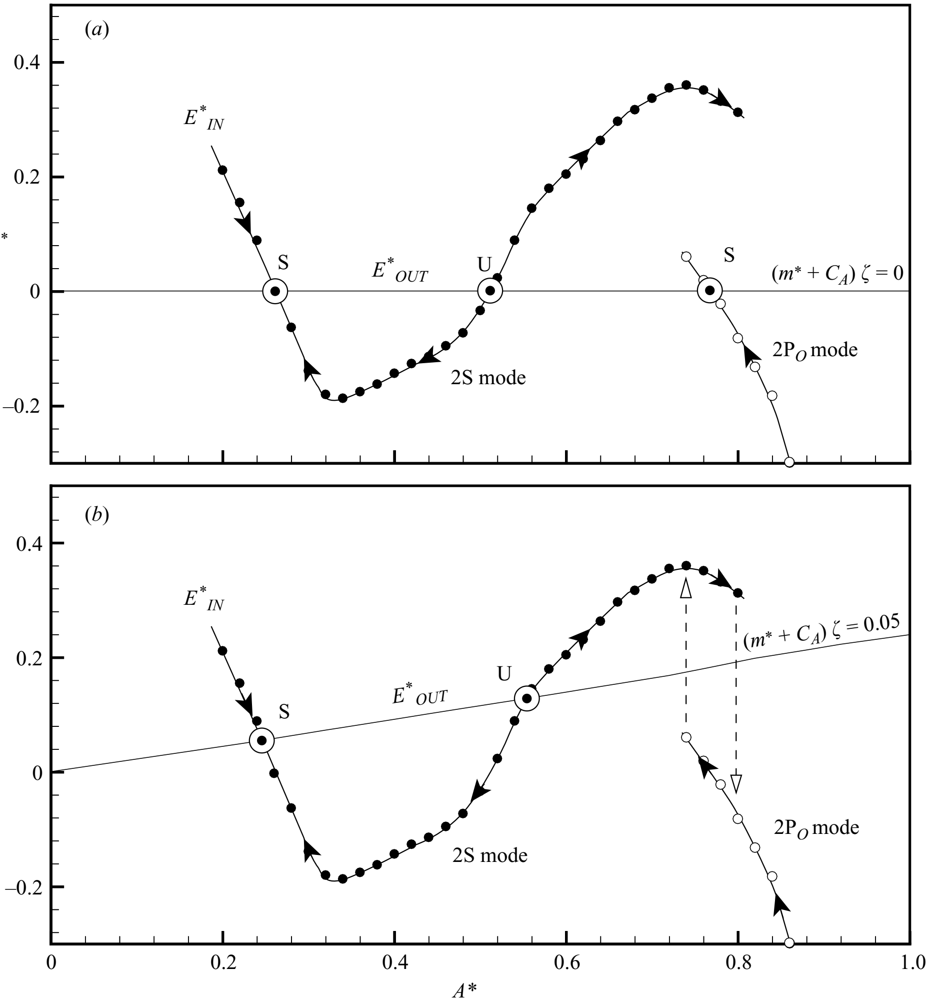

FIGURE 15. Energy portrait for $m^* = 10$, $U^* = 5.1$ showing distinct values of the fluid excitation (E^*_{IN}) for the 2S (●) and $2P_O$ (○) vortex-formation modes. (*a*) For low mass damping there are three equilibria (⊙). (*b*) For moderate mass damping, there is no stable-equilibrium point at the upper branch amplitude. Instead, the amplitude will vary between about $A^* = 0.74$ and $A^* = 0.8$.

will also be very slightly different for the two modes, but for simplicity we have kept an average value in this overlap regime). For the higher mass damping chosen here $[(m^* + C_A)\zeta = 0.09]$, three solutions are found as shown earlier in figure 14. For our lowest selected mass damping here $[(m^* + C_A)\zeta = 0]$, the high-amplitude stable solution would exhibit the $2P_O$ wake mode, in figure 15(*a*), yielding an upper branch, as observed typically in free-vibration experiments.

A particularly interesting case occurs if one has an intermediate mass damping in figure 15(*b*), since there is no equilibrium point to give a steady upper-branch amplitude. If the system has an amplitude above 0.6 or so, and we have the 2S mode of vortex formation, the energy into the system will be greater than the energy lost to damping, and the amplitude will increase until the system enters the $2P_O$ regime. The fluid excitation will drop, but it will now fall below the energy dissipated to damping, causing the amplitude to decrease until the vortex mode jumps back to the 2S mode.

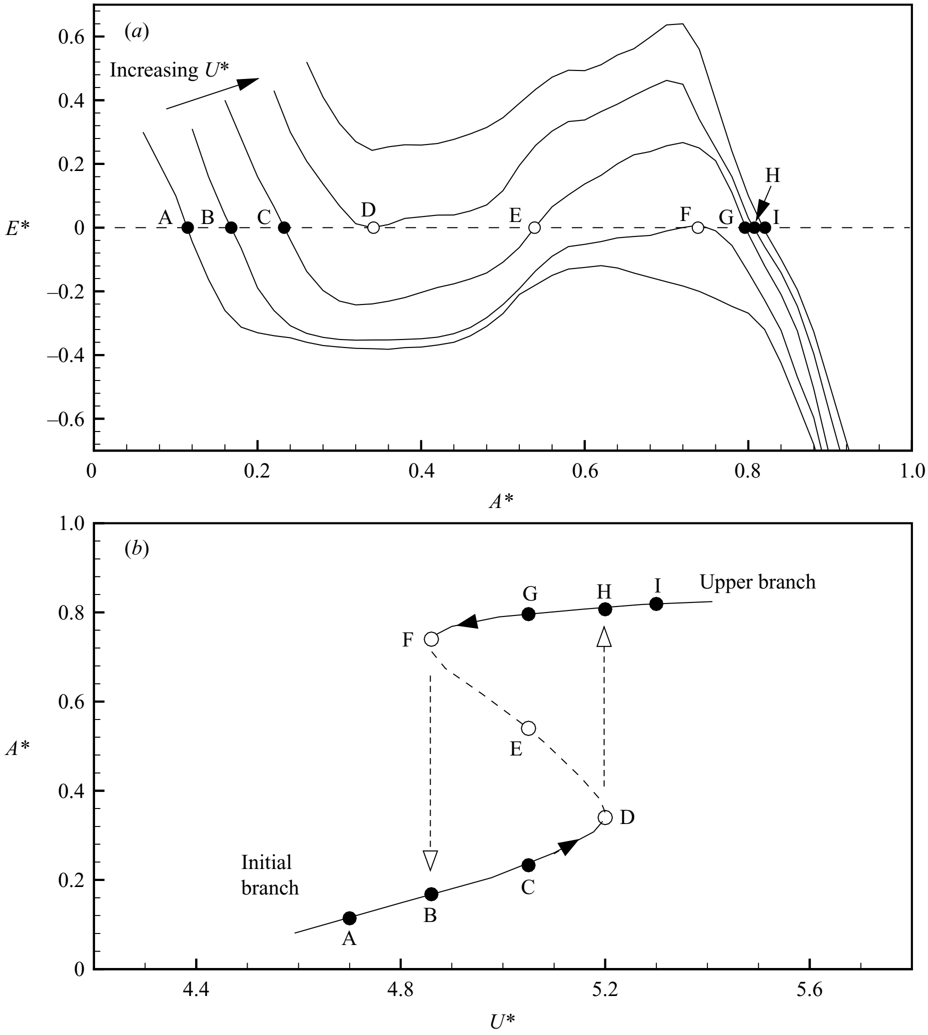

FIGURE 16. (*a*) Energy portraits and (*b*) amplitude response (*b*) for the hysteresis mode transition between the initial and upper branches for $m^* = 10$; E^*_{IN} curves are shown for $U^* = 4.70, 4.86, 5.05, 5.20$ and 5.30; ●, stable equilibria; ○, unstable equilibria.

In this manner, the cycle will repeat. Thus the normalized amplitude will fluctuate in an unsteady manner, remaining between about 0.72 and 0.8. This type of behaviour is actually observed in the free-vibration case, where the upper branch often shows oscillations that are less steady than found in the initial or lower branches (Khalak & Williamson 1996).

6.2. *Hysteresis between the Initial ↔ Upper branches*

In the free-vibration response of Govardhan & Williamson (2006), as shown in figure 11, there exists a hysteretic mode transition between the initial and upper response branches, around $U^* = 5.5$. This hysteresis, for such a low-mass-damping system, can readily be understood, if we employ a set of energy portraits over a small range of the normalized velocity, as shown in figure 16. For simplicity we will consider a system with zero damping so that all the equilibria will lie on the horizontal axis. (Also we will take an average of the fluid excitation in the region in which the 2S and $2\mathrm{P}_O$ modes overlap, simply to clarify the phenomena and avoid the small cyclic oscillations we saw in figure 15*b*.) Depending on the normalized velocity, there may be one stable-equilibrium solution or two stable solutions plus one unstable solution. The location of all these equilibrium solutions on a free-vibration amplitude-response plot are shown in figure 16(*b*).

We commence with a low velocity $U^*=4.70$, where only one solution exists, corresponding to the initial branch, shown as point A in figure 16(*b*). The reader should look back and forth between figures 16(*a*) and 16(*b*) while we discuss the hysteresis as follows. As we increase U^* to 4.86 and upwards to 5.05, a second stable-equilibrium point will appear on the upper branch (point G). Nevertheless, the system will remain on the initial branch (point C). Once the normalized velocity is increased to 5.20, the initial-branch equilibrium will disappear in a 'saddle-node bifurcation' (point D), and the amplitude will jump to the upper branch (point H). With further increase in U^*, the solution simply shifts along the upper branch (to point I and beyond). However, if the normalized velocity is decreased, the solution will remain on the upper branch, until that equilibrium disappears in another saddle-node bifurcation at $U^*=4.86$ (point F). The amplitude will then drop to the initial branch (point B), thus completing the hysteresis loop. In summary, the progression of points for increasing U^* is A–B–C–D–jump to H–I. For decreasing U^*, we have I–H–G–F–drop to B–A.

In the case of a free-vibration system with high mass damping, there are only two branches of response: an initial branch and a lower branch, as shown also in figure 11, with a hysteretic mode transition between them. From the contours presented here, such a hysteresis would not be predicted. However, Bishop & Hassan (1964) showed from their controlled-vibration 'amplitude cuts' that the location of the jump in magnitude and phase of fluid forcing (which we now know is due to a change in vortex-formation mode from 2S to 2P) depends on whether the frequency of vibration is increasing or decreasing. In our case we do not dynamically vary the frequency; so we cannot observe any hysteresis in the force contours. We expect that the precise location of the 2S–2P boundary will shift very slightly if the frequency (or wavelength) is dynamically increased or decreased and that this shift in the boundary is what causes the hysteresis between the initial and lower branches of a high-mass-damping response.

6.3. *Intermittent switching between Upper ↔ Lower branches*

In the free vibration of figure 11(*a*), there exists an intermittent switching between the upper and lower branches at velocities $U^*\sim 6$. If we look at the energy portrait for a normalized velocity cut ($U^*=6.3$) passing through the $2\mathrm{P}_O$–2P overlap region, there will be two curves of excitation energy E^*_{IN}, one for the each mode of vortex shedding, as shown in figure 17. (There will also be two E^*_{OUT} curves because the value of C_{EA} and thus f^* are slightly different for the two modes. This difference is extremely small (less than 1 %), and so we show an averaged line for simplicity.)

For low mass damping, as indicated in figure 17, if the vortex-shedding mode is $2\mathrm{P}_O$, then there will be one stable equilibrium at the upper-branch amplitude (around $A^*=0.8$). However, this equilibrium will only persist if the vortex-formation mode continues to be $2\mathrm{P}_O$. If the wake switches to a 2P mode, the fluid excitation will drop. This will cause the energy into the system to be less than the energy dissipated by damping, and therefore the amplitude will decrease until a new stable equilibrium for the 2P mode is reached, corresponding to a lower-branch amplitude (around $A^*=0.5$). Later in time, the vortex-formation mode could possibly switch back to

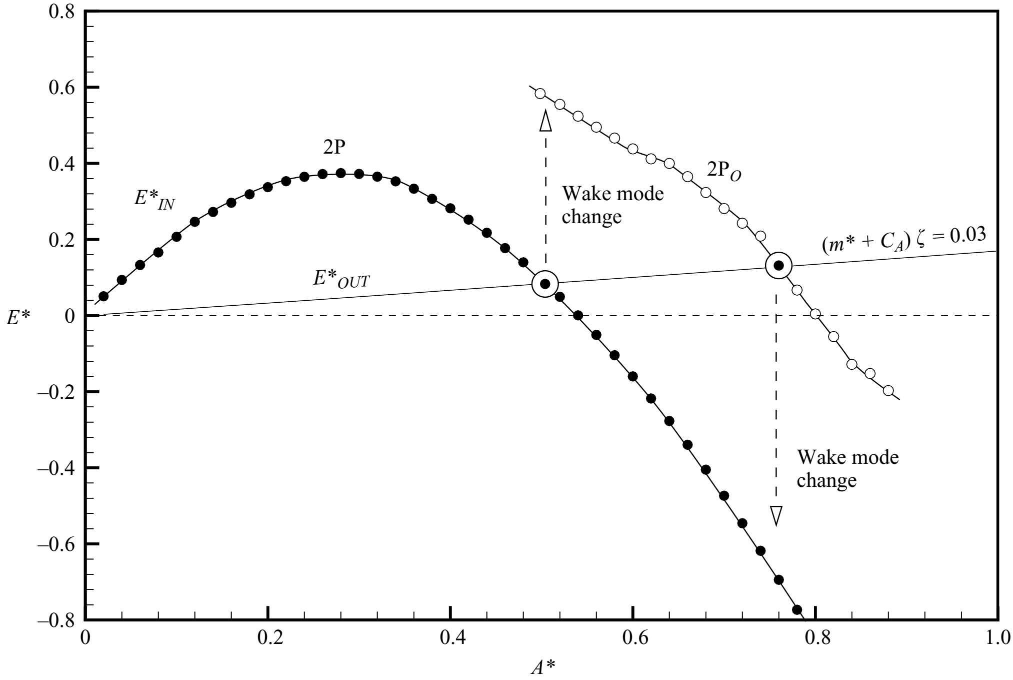

FIGURE 17. Energy portrait for $m^* = 10$, $U^* = 6.3$ (upper and lower branches), showing distinct values of the fluid excitation (E^*_{IN}) for the 2P (●) and 2P$_O$ (○) vortex-formation modes. Stable equilibria (⊙) exist for each vortex-formation mode, corresponding to the upper branch (2P$_O$) and lower branch (2P). A change in the mode causes a jump in the fluid excitation and therefore a change in amplitude.

2P$_O$, causing the amplitude to increase back towards the upper-branch amplitude. In this way, the amplitude could switch intermittently between the upper and lower branches, sometimes staying at one amplitude or the other for several cycles. This corresponds to what is actually observed in free-vibration systems, for example in Govardhan & Williamson (2000).

We emphasize that the switching phenomenon described here is fundamentally different from the unsteady behaviour which can occur in the 2S–2P$_O$ overlap region described in § 6.1 and shown in figure 15(*b*). In the 2S–2P$_O$ overlap region the variation in amplitude is much smaller, and no steady motion is possible for either vortex-formation mode. In the 2P$_O$–2P overlap region, the difference in amplitude is quite dramatic (appearing as a jump between an upper branch and a lower branch), and we find steady amplitude motion can occur, so long as the vortex wake mode remains the same.

7. Defining the regime in which free vibration is possible

The evaluation of fluid forcing, throughout the amplitude–wavelength plane, enables us to determine the regimes in which free vibration can occur, of course under the assumption that such motion is approximately sinusoidal. The classical understanding, presented in figure 18(*a*), is that the region of possible free vibration is the intersection of the positive excitation region and the synchronized wake region. However, we have found, in this paper, that there exist conditions at which, even though the fluid

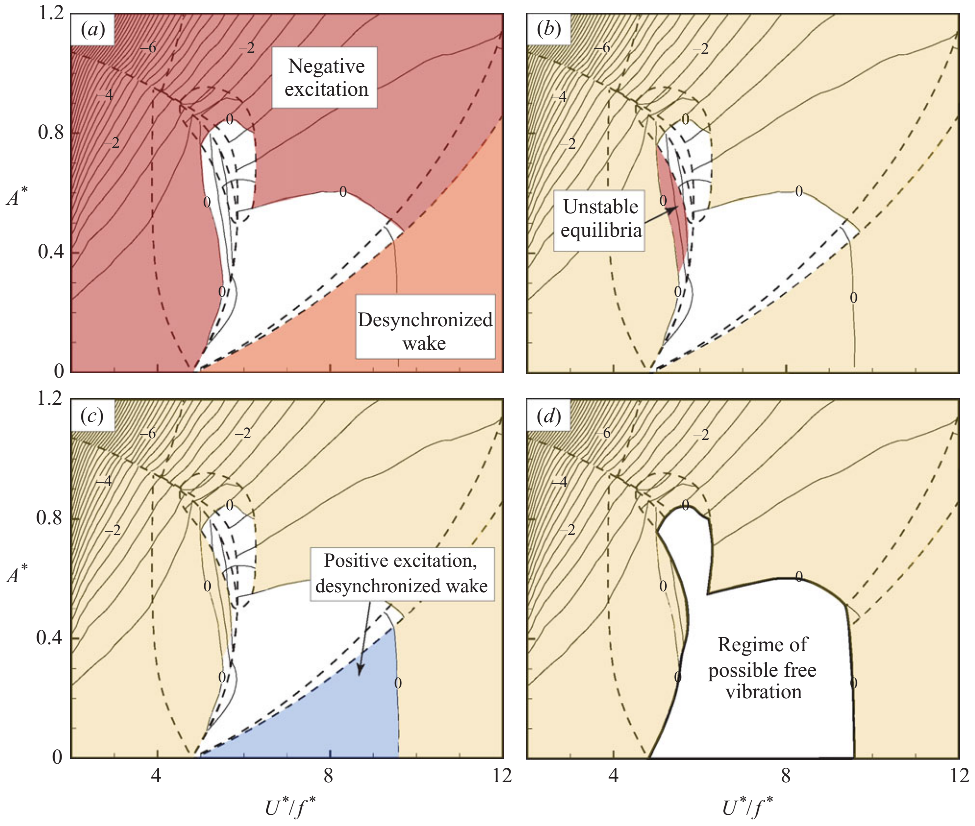

FIGURE 18. Map of where free vibration can occur in the amplitude–velocity plane for $m^* = 10$ (shown with contours of $C_Y \sin\phi$). (*a*) Region in which the wake is desynchronized from the cylinder motion and region in which the fluid excitation is negative. (*b*) Region in which the equilibria are unstable. (*c*) Region in which positive excitation exists, even with a desynchronized wake. (*d*) Regime of possible free vibration: the fluid excitation is positive, and the solutions to the equation of motion are stable.

excitation is positive and the equations of motion are satisfied, the equilibrium solutions are unstable. We therefore remove the area in the amplitude–wavelength plane, where these solutions are unstable, to yield our regime of possible free vibration, in figure 18(*b*).

We may further point out that vortex-induced motion can occur in the desynchronized region if there is some positive fluid excitation at the oscillation frequency. The fluid forcing in the desynchronized region has a large component at the (higher) natural vortex-shedding frequency, but in fact it also exhibits a smaller force component at the oscillation frequency, as discussed in more detail in Morse & Williamson (2009*a*). Thus, one might expect that free vibration in this region would have distinctly non-sinusoidal motion. However, since the effect of fluid forcing on vibration amplitude is greatly diminished for frequencies away from the oscillation frequency, the higher-frequency-forcing component can have a negligible effect on the overall body dynamics. Therefore, in our search for the regime of possible free vibration, we add in the region of positive excitation within the desynchronized regime, in figure 18(*c*). Finally, we may present the overall regime of possible free vibration in figure 18(*d*), which satisfies the requirements that not only is the fluid excitation is positive, but also the amplitude solutions are stable.

8. Conclusions

In this paper, we have presented new measurements of fluid force on a cylinder that oscillates under controlled vibration, transverse to a flow. We have presented these new results in the form of high-resolution force-contour plots within the plane of normalized amplitude and wavelength (A^*, λ^*), for the Reynolds numbers $Re = 4000$ and $Re = 12\,000$. We have identified distinct boundaries and fluid-force regimes in the amplitude–wavelength plane, based solely on the force measurements. Indeed, we find good agreement between the shapes of the regimes evaluated from force measurements in the present work and the regimes of vortex-formation modes identified from flow visualization in the map of regimes by Williamson & Roshko (1988). By measuring the wake vorticity, we find vortex-formation modes that correspond well with those in the Williamson–Roshko map, namely the 2S and 2P modes, as well as with the asymmetric P + S mode.

The present high-resolution contour plots have enabled us to discover a new high-amplitude regime, in the amplitude–wavelength plane, which overlaps the boundary between the 2S and 2P regimes. Vorticity measurements identify the new vortex-formation mode to be similar to the 2P mode but where the second vortex of each pair is much weaker than the first vortex, in what we define as the '$2\mathrm{P}_{OVERLAP}$' or '$2\mathrm{P}_O$' mode. During an experiment, the vortex-formation mode and fluid force can switch intermittently between the $2\mathrm{P}_O$ and 2P modes, even when the amplitude and frequency are kept constant. The switch in vortex-formation mode can cause a large jump in the fluid excitation, which would lead to a jump in amplitude for a free-vibration response, as found in direct measurements on elastically mounted bodies.

Employing the force-contour data, we are able to predict the response of a freely vibrating cylinder. This prediction agrees well with direct measurements from free-vibration experiments, for the three-branch response of a low-mass-damping system and for the two-branch response of a system with high mass damping. We are also able to accurately recreate the 'modified Griffin plot' of peak amplitude versus mass damping at both $Re = 4000$ and $Re = 12\,000$ (shown in the appendix), and our data also agrees well with the plot of peak amplitude as a function of *Re*, compiled in the recent work of Govardhan & Williamson (2006).

In order to study the stability of equilibrium amplitude solutions and to better understand the mode transitions between solution branches of the free-vibration response, we have introduced the concept of an 'energy portrait'. We define such an energy portrait as a plot of the excitation energy into the system and the energy out of the system dissipated by damping, as a function of amplitude, as we keep normalized flow velocity constant. The energy portrait allows us to identify equilibrium points, where there is a balance of energy transfer into the system (E^*_{IN}) and out of the system (E^*_{OUT}), and to determine the stability of these equilibrium points, as follows:

$$\begin{aligned} \text{stable,} \quad & \mathrm{d}E^*/\mathrm{d}A^* < 0, \\ \text{unstable,} \quad & \mathrm{d}E^*/\mathrm{d}A^* > 0, \end{aligned}$$

where E^* is the net energy ($E^*_{IN} - E^*_{OUT}$) transferred into the body motion.

In the vicinity of the transition between the initial and upper response branches found in free vibration, for low mass damping, the fluid excitation follows an 'S-like' shape, leading to multiple equilibria in the energy portrait. We are able to explain the existence of hysteresis, found in free vibration, on the basis of a set of energy portraits, where we identify saddle-node bifurcations and where we may identify stable and unstable solutions. On the other hand, the transition from the upper branch to the lower branch of free-vibration response involves an intermittent switching between the modes. We may explain this phenomenon by considering the overlap of two mode regimes in the amplitude–wavelength plane. The vortex formation is able to switch intermittently as a function of time and induces jumps between two stable amplitude solutions, one corresponding with the $2P_O$ mode, with higher excitation energy, and the other corresponding with the 2P mode of vortex formation, with lower excitation energy. In essence, the hysteresis between modes occurs due to the shape of the fluid-excitation contours in the amplitude–wavelength plane, while the intermittent-switching transition occurs because there is an overlap of mode regimes in this plane.

As a further point, we may clearly define the region in the amplitude–wavelength plane that would admit free vibration. The requirements for free vibration have generally been assumed to be a synchronized wake and a positive fluid excitation. However, through our energy portraits, we have identified a regime for unstable equilibria where steady free vibration is not possible, which must therefore be removed from the region of possible free vibration. We should also note that vortex-induced vibration can occur if there is an area of positive excitation even within the regime of the desynchronized wake. Therefore, our complete regime for free vibration in the amplitude–wavelength plane satisfies two principal criteria; namely the existence of net positive fluid excitation and stability of the equilibrium amplitude solutions.

Finally, we now return to several questions that were posed at the start of the introduction, and we put forward here some responses to those questions.

(i) *What is the cause of the hysteresis between the initial and upper branches of response?* This is related to the fact that the energy portrait exhibits an S-like shape, yielding multiple solutions, two of which are stable for a particular flow velocity.

(ii) *What causes intermittent switching between the upper and lower branches?* We now understand this as caused by the overlap of two vortex-formation modes for the same amplitude and wavelength of the body's vibration, with the possibility that the wake flow intermittently switches between vortex-formation modes.

(iii) *Which modes of vortex formation can cause vortex-induced vibration?* Apparently the modes causing vibration, in this regime of the Reynolds number, are not only the well-known 2S and 2P modes but also the overlap $2P_O$ mode, discovered in this work. However, we also predict vibration in the 'desynchronized' vortex mode regime.

(iv) *What is the relation between the modes of vortex formation and the fluid excitation?* The maps of vortex-induced forces, compiled here, demonstrate clear regimes and boundaries in the amplitude–wavelength plot, which directly correspond to the different modes of vortex formation, originally found in the map of Williamson & Roshko (1988). The positive excitation is observed for the 2S, 2P and $2P_O$ modes and is found to change sign with only very minor changes to the phase of the fluid forcing. We also find in this work that the 'desynchronized' vortex-formation regime can still yield net positive excitation and thereby deliver body vibration.

(v) *To what extent can controlled vibration be used to accurately predict the behaviour of a freely vibrating cylinder?* Previously there was some debate, for a number of years, that controlled vibration was not always a good predictor of free vibration. However, the conclusion here is that so long as the experimental conditions of the controlled vibration match well those for the free vibration (end conditions, etc.), and the controlled vibrations are of sufficient high resolution, the prediction can be very good. In fact, not only are the steady-state vibrations very well predicted, but the non-steady and transient vibrations can also be well predicted, and for clarity and brevity this is presented in a separate and subsequent contribution (Morse & Williamson 2009*b*).

The support from the Ocean Engineering Division of ONR, monitored by Dr Tom Swean, is gratefully acknowledged (ONR contract no. N00014-04-1-0031 and N00014-07-1-0303). The authors would also like to thank Matt Horowitz and Raghu Govardhan for their extremely helpful inputs to this research.

Appendix. The effect of the Reynolds number on the fluid-force contours and prediction of the 'modified Griffin plot'

A basic question one might ask is how dependent are the fluid-forcing contours in the amplitude–wavelength plane on the value of the Reynolds number used for the plot. We have conducted another complete set of experiments to obtain force contours at $Re = 12\,000$. We present as an example, in figure 19, contours of the fluid excitation ($C_Y \sin\phi$). Interestingly, the same fluid-forcing regimes are found for the $Re = 12\,000$ case as we found here for $Re = 4000$, including the 2P_O mode. The general shape of the fluid-excitation contours is also quite similar, suggesting that the same general conclusions made in the present paper remain valid over a whole range of the Reynolds number. One should note that we are not in a position to observe the P + S regime because the high-amplitude, low-wavelength (high-frequency) region of the amplitude–wavelength plot (top left corner) exceed the limits of our facilities at this *Re*. The major effect of increased *Re* appears to be a vertical stretching of the 2S and 2P_O regimes. The zero-excitation contour in the 2P_O regime has a distinctly higher amplitude. This means that one expects a higher peak-amplitude response for very small (or zero) damping as the Reynolds number is increased. On the other hand, the location of the zero-excitation contour for the 2P region, in the amplitude–wavelength plane, remains virtually unchanged as the Reynolds number is increased.

It is interesting that, in fact, our controlled-vibration contours at $Re = 4000$ and 12 000 can also be used to predict the peak-amplitude vibration response as a function of mass damping, in what is called a modified Griffin plot. Such a plot, which was presented by Govardhan & Williamson (2006), shows the effect of mass damping, as well as that of the Reynolds number, on the peak-amplitude response in free vibration, and involves a collapse of such extensive data into a single curve. Here we choose to plot the two Reynolds numbers separately to indicate the effect of the Reynolds number more directly. We can compute these data as curves in figure 20(*a*), using the approach of § 5.

For both Reynolds numbers, the controlled-vibration contours yield good agreement with the empirical formula, taking into account mass damping as well as the Reynolds number, deduced by Govardhan & Williamson (2006),

$$A^* = (1 - 1.2\alpha + 0.30\alpha^2)\log(0.41 Re^{0.36}). \qquad \text{(A 1)}$$

The predicted peak amplitude is slightly lower than the measured free-vibration amplitude for the $Re = 4000$ case, but the shape of the trend is well predicted. The agreement with free-vibration peak-amplitude data at $Re = 12\,000$ appears to be good. We also find the location, in our amplitude–wavelength plane, at which the excitation energy ($C_Y \sin\phi$) is zero, for both $Re = 4000$ and $Re = 12\,000$. These values predict the peak-response amplitude, which could be found in free vibration if the damping is brought to zero. A subsequent inclusion of our data on to the plot of peak response

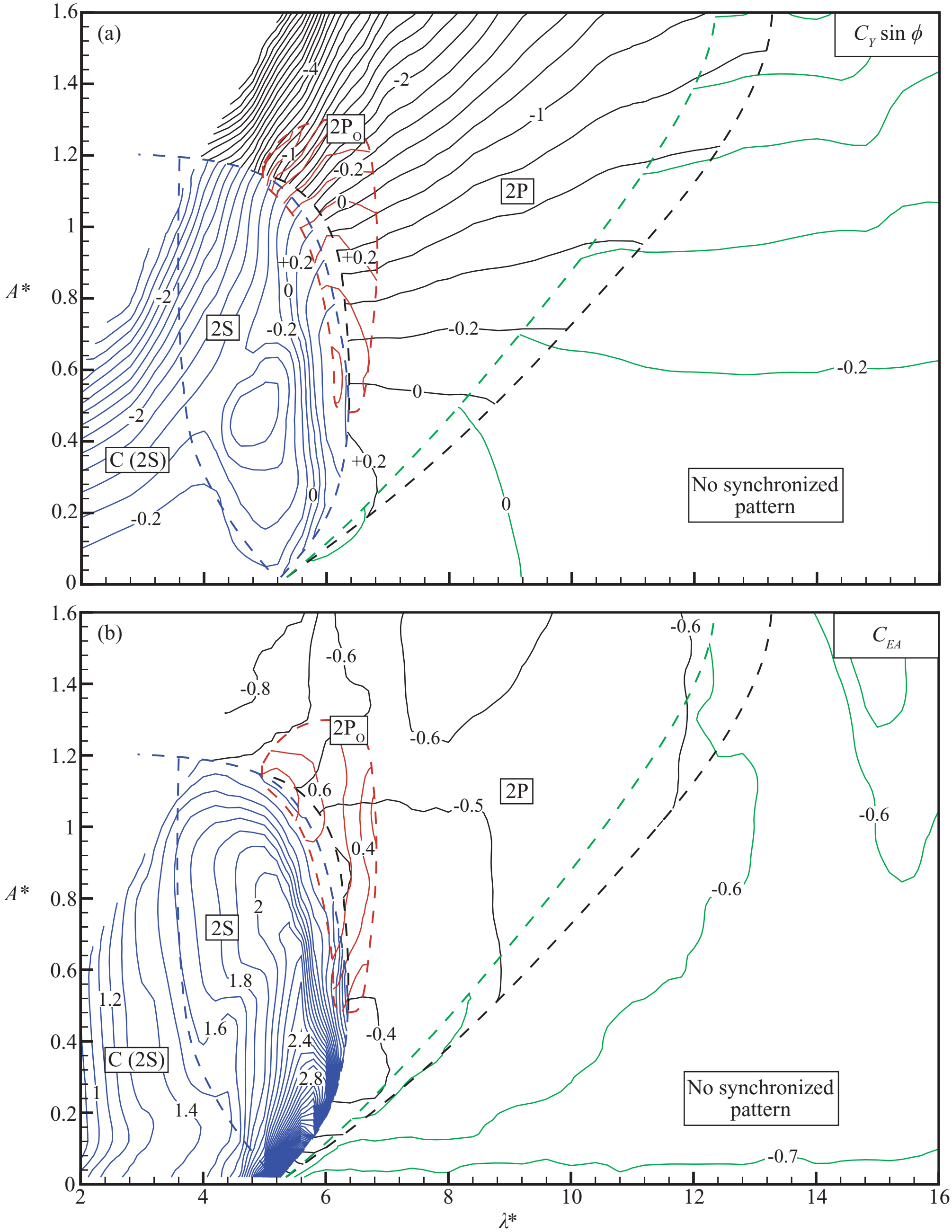

FIGURE 19. Contours of (*a*) the force in phase with velocity, $C_Y \sin\phi$, normalized 'fluid excitation', and (*b*) the effective added mass, C_{EA}, for $Re = 12\,000$. Boundaries between modes are indicated by the dashed lines. We could not obtain data in the upper left corner due to the limits of our facilities. Contour interval is 0.2 for $C_Y \sin\phi$ and 0.1 for C_{EA}.

(for zero damping) as a function of the Reynolds number, compiled for free vibration experiments by Govardhan & Williamson (2006),

$$A^*_{PEAK} = \log(0.41 Re^{0.36}), \tag{A 2}$$

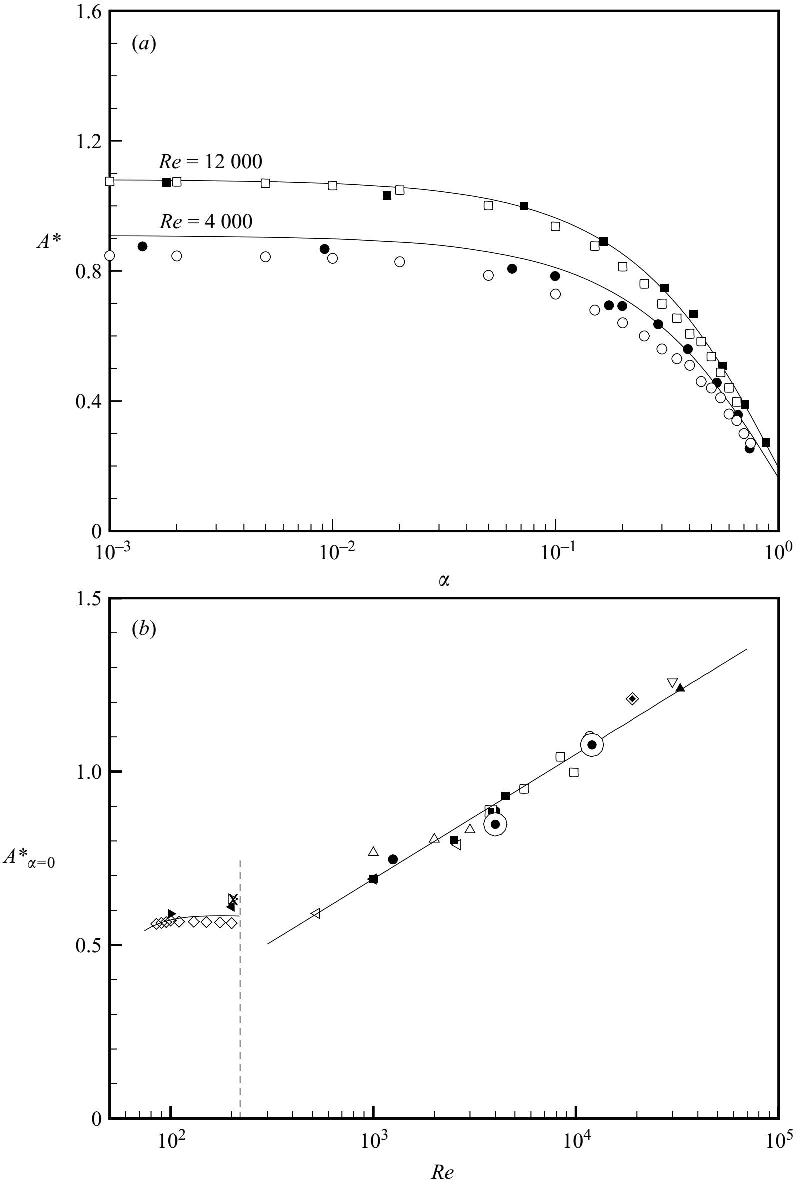

FIGURE 20. (a) The 'Griffin' plot of peak amplitude versus mass damping, α: ●, $Re = 4000$; ■, $Re = 12\,000$, free-vibration results from Govardhan & Williamson (2006); ○, $Re = 4000$; □, $Re = 12\,000$, predicted peak amplitude from present controlled-vibration data. The lines indicate the best fit for a range of experiments, deduced by Govardhan & Williamson (2006): $A^* = (1 - 1.2\alpha + 0.30\alpha^2)\log(0.41Re^{0.36})$. ($b$) Peak amplitude at zero mass damping versus Re for a wide range of experiments, taken from Govardhan & Williamson (2006); symbols are given in table 3 of that paper (not reproduced here); ⊙, our present predictions from controlled vibration.

is shown in figure 20(b), indicating good agreement. We should also note that the peak amplitudes are reasonably independent of blockage in this plot, at least over the regime of blockage ratios, $D/W = 5$–15 % (where $W =$ test-section width).

REFERENCES

Bearman, P. W. 1984 Vortex shedding from oscillating bluff bodies. *Annu. Rev. Fluid Mech.* **16**, 195–222.

Bishop, R. E. D. & Hassan, A. Y. 1964 The lift and drag forces on a circular cylinder oscillating in a flowing fluid. *Proc. R. Soc. Lond.* A **227**, 51–75.

Brika, D. & Laneville, A. 1993 Vortex-induced vibrations of a long flexible circular cylinder. *J. Fluid Mech.* **250**, 481–508.

Carberry, J., Govardhan, R., Sheridan, J., Rockwell, D. & Williamson, C. H. K. 2004 Wake states and response branches of forced and freely oscillating cylinders. *Eur. J. Mech.* B **23**, 89–97.

Carberry, J., Sheridan, J. & Rockwell, D. 2001 Forces and wake modes of an oscillating cylinder. *J. Fluids Struct.* **15**, 523–532.

Carberry, J., Sheridan, J. & Rockwell, D. 2003 Controlled oscillations of a cylinder: a new wake state. *J. Fluids Struct.* **17**, 337–343.

Carberry, J., Sheridan, J. & Rockwell, D. 2005 Controlled oscillations of a cylinder: forces and wake modes. *J. Fluid Mech.* **538**, 31–89.

Feng, C. C. 1968 The measurement of vortex-induced effects in flow past stationary and oscillating circular and D-section cylinders. Master's thesis, University of British Columbia, Vancouver, BC, Canada.

Gopalkrishnan, R. 1993 Vortex-induced forces on oscillating bluff cylinders. PhD thesis, Massachusetts Institute of Technology, Cambridge, MA.

Govardhan, R. & Williamson, C. H. K. 2000 Modes of vortex formation and frequency response of a freely vibrating cylinder. *J. Fluid Mech.* **420**, 85–130.

Govardhan, R. & Williamson, C. H. K. 2006 Defining the 'modified Griffin plot' in vortex-induced vibration: revealing the effect of Reynolds number using controlled damping. *J. Fluid Mech.* **561**, 147–180.

Griffin, O. M. 1980 Vortex-excited crossflow vibrations of a single cylindrical tube. *Trans. ASME, J. Press. Vessel Technol.* **102**, 158–166.

Griffin, O. M. & Ramberg, S. E. 1982 Some recent studies of vortex shedding with application to marine tubulars and risers. *J. Energy Resource Technol.* **104**, 2–13.

Hover, F. S., Techet, A. H. & Triantafyllou, M. S. 1998 Forces on oscillating uniform and tapered cylinders in crossflow. *J. Fluid Mech.* **363**, 97–114.

Khalak, A. & Williamson, C. H. K. 1996 Dynamics of a hydroelastic cylinder with very low mass and damping. *J. Fluids Struct.* **10**, 455–472.

Khalak, A. & Williamson, C. H. K. 1999 Motions, forces and mode transitions in vortex-induced vibrations at low mass-damping. *J. Fluids Struct.* **13**, 813–851.

Leontini, J. S., Stewart, B. E., Thompson, M. C. & Hourigan, K. 2006*a* Predicting vortex-induced vibration from driven oscillation results. *Appl. Math. Model.* **30**, 1096–1102.

Leontini, J. S., Stewart, B. E., Thompson, M. C. & Hourigan, K. 2006*b* Wake state and energy transitions of an oscillating cylinder at low Reynolds number. *Phys. Fluids* **18**, 067101.

Lighthill, J. 1986 Wave loading on offshore structures. *J. Fluid Mech.* **173**, 667–681.

Mercier, J. A. 1973 Large amplitude oscillations of a circular cylinder in a low speed stream. PhD thesis, Stevens Institute of Technology, Hoboken, NJ.

Morse, T. L. & Williamson, C. H. K. 2006 Employing controlled vibrations to predict fluid forces on a cylinder undergoing vortex-induced vibration. *J. Fluids Struct.* **22**, 877–884.

Morse, T. L. & Williamson, C. H. K. 2009*a* Fluid forcing, wake modes, and transitions for a cylinder undergoing controlled oscillation. *J. Fluids Struct.* **25**, 697–712.

Morse, T. L. & Williamson, C. H. K. 2009*b* Steady, unsteady, and transient vortex-induced vibration predicted using controlled motion data. *J. Fluid Mech.* (submitted).

Ongoren, A. & Rockwell, D. 1988 Flow structure from an oscillating cylinder. Part 2. Mode competition in the near wake. *J. Fluid Mech.* **191**, 225–245.

Parkinson, G. 1989 Phenomena and modelling of flow-induced vibrations of bluff bodies. *Progr. Aerosp. Sci.* **26**, 169–224.

Sarpkaya, T. 1977 Transverse oscillations of a circular cylinder in uniform flow. Part I. *Tech Rep.* NPS-69SL77071. Naval Postgraduate School, Monterey, CA.

Sarpkaya, T. 1979 Vortex-induced oscillations. *J. Appl. Mech.* **46**, 241–258.

Staubli, T. 1983 Calculation of the vibration of an elastically mounted cylinder using experimental data from forced vibration. *ASME J. Fluids Engng* **105**, 225–229.

Willden, R. H. J., McSherry, R. J. & Graham, J. M. R. 2007 Prescribed cross-stream oscillations of a circular cylinder at laminar and early turbulent Reynolds numbers. In *Fifth Conference on Bluff Body Wakes and Vortex-Induced Vibration (BBVIV-5)*, Costa do Sauipe, Brazil.

Williamson, C. H. K. & Govardhan, R. 2004 Vortex-induced vibrations. *Annu. Rev. Fluid Mech.* **36**, 413–455.

Williamson, C. H. K. & Roshko, A. 1988 Vortex formation in the wake of an oscillating cylinder. *J. Fluids Struct.* **2**, 355–381.